JGR Space Physics

RESEARCH ARTICLE
10.1029/2024JA032550

**Key Points:**

- A new expression incorporating Modified Apex coordinates for calculating the Rayleigh-Taylor (R-T) instability growth rate has been established
- The simulation of R-T growth rate using Whole Atmosphere Model and Ionosphere Plasmasphere Electrodynamic model closely resembles the bubble occurrence observed by satellites
- The R-T instability is primarily driven by the eastward electric field, which is correlated with the pre-reversal enhancement vertical drift

**Supporting Information:**

Supporting Information may be found in the online version of this article.

**Correspondence to:**

C.-Y. Huang,
chun.yen@colorado.edu

**Citation:**

Huang, C.-Y., Fang, T.-W., Richmond, A. D., Fuller-Rowell, T. J., & Liu, J.-Y. (2024). New expression of the field-line integrated Rayleigh-Taylor instability growth rate. *Journal of Geophysical Research: Space Physics*, *129*, e2024JA032550. https://doi.org/10.1029/2024JA032550

Received 16 FEB 2024
Accepted 5 AUG 2024

**Author Contributions:**

**Conceptualization:** Chun-Yen Huang, Tzu-Wei Fang, Arthur D. Richmond
**Data curation:** Chun-Yen Huang, Tzu-Wei Fang
**Formal analysis:** Chun-Yen Huang
**Funding acquisition:** Tzu-Wei Fang, Timothy J. Fuller-Rowell
**Investigation:** Chun-Yen Huang, Tzu-Wei Fang, Arthur D. Richmond, Timothy J. Fuller-Rowell, Jann-Yenq Liu
**Methodology:** Chun-Yen Huang, Arthur D. Richmond
**Project administration:** Tzu-Wei Fang, Timothy J. Fuller-Rowell
**Resources:** Tzu-Wei Fang
**Software:** Tzu-Wei Fang

# New Expression of the Field-Line Integrated Rayleigh-Taylor Instability Growth Rate

**Chun-Yen Huang**[1,2], **Tzu-Wei Fang**[3], **Arthur D. Richmond**[4], **Timothy J. Fuller-Rowell**[1,3], and **Jann-Yenq Liu**[2]

[1]Cooperative Institute for Research in Environmental Sciences, University of Colorado Boulder, Boulder, CO, USA, [2]Department of Space Science and Engineering, National Central University, Taoyuan City, Taiwan, [3]Space Weather Prediction Center, National Oceanic and Atmospheric Administration, Boulder, CO, USA, [4]High Altitude Observatory, National Center for Atmospheric Research, Boulder, CO, USA

**Abstract** An expression of Rayleigh-Taylor (R-T) instability growth rate based on the field-line integrated theory is newly established. This expression can be directly utilized in ionosphere models with magnetic flux tube structure based on Modified Apex Coordinates. The R-T instability growth rates are calculated using the thermospheric and ionospheric conditions based on the coupled Whole Atmosphere Model and Ionosphere Plasmasphere Electrodynamic model (WAM-IPE). The parameters used in this calculation include the field-line integrated conductivities and currents, which consider the Quasi-Dipole Coordinates and the modifications to the equations of electrodynamics. Detailed description of the new formulas and comprehensive analyses of diurnal, longitudinal, and seasonal variations of the R-T instability growth rate are carried out. The dependencies of growth rates on pre-reversal enhancement (PRE) vertical drifts and solar activity are also examined. The results show that pronounced R-T growth rates are captured between 18 and 22 local time (LT) when strong PRE occurs in the equatorial ionosphere. The simulated R-T growth rate increases with increasing solar activity levels and demonstrates strong correlations with the angle between the sunset terminator and the geomagnetic field line. These results are consistent with plasma irregularity occurrence rates shown in various satellite observations, suggesting that the newly developed R-T growth rate calculation can effectively capture the probability of irregularities by considering the changes along magnetic flux-tubes in the ionosphere. Since the WAM-IPE is running in operation at National Oceanic and Atmospheric Administration Space Weather Prediction Center, the new calculations can be potentially implemented in the near future to provide forecasted information of the R-T growth rate.

## 1. Introduction

The Rayleigh-Taylor (R-T) instability is considered to be the key contributor in creating severe equatorial spread *F* (ESF) and equatorial plasma bubble (EPBs) at low latitudes (Booker & Wells, 1938; Dungey, 1956; Haerendel, 1973; Sultan, 1996). Some other instabilities can also induce the occurrence of plasma irregularities. The $\vec{E} \times \vec{B}$ gradient drift instability plays a role for high-latitude ionospheric irregularities (Keskinen & Ossakow, 1983; Rathod et al., 2021), the rapid structuring of barium clouds (Linson & Workman, 1970), and turbulence in equatorial electrojet (Hu & Bhattacharjee, 1999; Hysell & Chau, 2023; Ossakow, 1979). The electrostatic Kelvin-Helmholtz instability/collisional shear instability produces large-scale waves in the collisional regime in the equatorial region, acting as an effective seed for the R-T instability (Hysell & Kudeki, 2004; Hysell et al., 2006; Keskinen et al., 1988). Furthermore, the Perkins instability contributes to the generation of medium-scale traveling ionospheric disturbances, causing field-aligned irregularities in the mid-latitude *E* region and *F* region (Fukao et al., 1991; Kelley & Fukao, 1991; Klevans & Imel, 1978; Otsuka et al., 2007; Perkins, 1973).

In the equatorial ionosphere, the occurrence of EPBs is influenced by the initial condition of R-T instability within the highly stratified *F* region ionosphere after sunset, characterized by relatively higher plasma density above the lower density region. $O^+$ ions dominate the post-sunset *F* region plasma. They have a much lower reaction rate than that of the molecular ions that are dominant in the *E* region, which results in a significantly longer lifetime for $O^+$ ions compared to molecular ions (Kelley, 2009). As a result, the ionosphere forms a steep vertical plasma density gradient due to the relatively higher plasma density in the *F* region compared to that in the *E* region. The strong vertical plasma gradient is then disturbed by factors such as atmospheric gravity waves, serving as a

**Supervision:** Tzu-Wei Fang, Arthur D. Richmond, Timothy J. Fuller-Rowell, Jann-Yenq Liu
**Validation:** Chun-Yen Huang
**Visualization:** Chun-Yen Huang
**Writing – original draft:** Chun-Yen Huang
**Writing – review & editing:** Tzu-Wei Fang, Arthur D. Richmond, Timothy J. Fuller-Rowell, Jann-Yenq Liu

seeding mechanism to generate plasma irregularities and EPBs (e.g., Kelley et al., 1981; Rottger, 1973; Tsunoda, 1981). These EPBs rapidly rise through the ionospheric *F* region and develop irregularities in different scale-sizes.

To investigate the EPBs onset condition, the linear R-T growth rates based on both a local approximation and a flux tube integrated formulation have been previously studied in various theoretical and experimental works (Hanson et al., 1986; Huba, 2022; Hysell, 2000; Lee, 2006; Mendillo et al., 1992; Ossakow et al., 1979, 1981; Sultan, 1996; Zalesak & Ossakow, 1982). Ossakow et al. (1979) calculated the local linear growth rate and simulated the nonlinear evolution of the collisional R-T instability using modeled electron density profiles and atmospheric quantities. Hanson et al. (1986) estimated the local linear growth rate with the drift term to examine the effect of vertical drift on the R-T instability. Lee (2006) carried out a term analysis in the local linear growth rate equation on the magnitude of growth rate using an entire year of Jicarmaca digisonde observations and MSIS-90 model (Hedin, 1991). Huba (2022) presented the influences of ion inertia and acceleration forces in both local theory and flux-tube integrated theory. Due to the near-equipotentiality of magnetic field lines, Haerendel (1973) suggested that the "flux-tube integrated" theory would be more appropriate for studying the ESF at low latitudes.

Building on the work of Haerendel (1973) and Haerendel et al. (1992), Sultan (1996) proposed a general expression of linear field-line integrated R-T instability growth rate, and this expression has been utilized to formulate forecasting approaches aimed at predicting the occurrence of EPB in recent studies (e.g., Carter et al., 2014a, 2014b; Wu, 2015). Establishing the relationship between EPBs and R-T growth rates will significantly improve our forecast capability through understanding the underlying physics dominating the formation of plasma irregularities. Wu (2015) conducted a comparison between the occurrence of EPB observed by DMSP satellites and the R-T growth rate calculated using the Thermosphere Ionosphere Electrodynamics General Circulation Model (TIEGCM) (Qian et al., 2014; Richmond et al., 1992) and demonstrated the potential of using the R-T growth rate to study the climatology and morphology of EPBs.

The climatology of EPBs often involves the analysis of the post-sunset layer rise of the equatorial *F* region (Tsunoda et al., 2018). The eastward electric field intensifies prior to its reversal toward a westward direction after sunset, a phenomenon known as the pre-reversal enhancement (PRE) which causes a large upward plasma drift. The enhancement of the upward plasma drift is believed to be one of the main controlling factors for the generation of EPBs (Abdu et al., 1981; Basu et al., 1996; Farley et al., 1970, 1986; Fejer et al., 1999). PRE drift velocity increases with increasing solar activity and is inversely proportional to nighttime *E* region electron densities (Fesen et al., 2000). The PRE strength and the occurrence of EPBs can also be enhanced under particular conditions. When the solar terminator is aligned with magnetic field lines, the simultaneous decrease of *E* region conductivity in both hemispheres leads to a strong vertical drift (Tsunoda, 1985). Consequently, the occurrence rates of EPBs frequently peak during the equinoxes in most longitudinal sectors and in the December solstice in the American sector (Gentile et al., 2006; C. Y. Huang et al., 2022; Su et al., 2006).

In this study, based on the flux-tube integrated theory, a new expression for the linear R-T instability growth rate is developed. This expression incorporates non-dipolar distortions of the geomagnetic field as represented in magnetic apex coordinates (Richmond, 1995) enabling us to directly compute a more accurate R-T instability growth rate using the existing formula of field-line integrated conductivities and currents described in Richmond (1995). The global distribution of the new R-T growth rate in various seasons and longitudes and its dependencies on the PRE and solar activity are evaluated using the coupled Whole Atmosphere Model-Ionosphere Plasmasphere Electrodynamics (WAM-IPE) in this study.

## 2. WAM-IPE Model

The WAM is a General Circulation Model (GCM) of the neutral atmosphere (Akmaev et al., 2008; Fuller-Rowell et al., 2008) based on the previously operational Global Forecast System General Spectral Model at National Oceanic and Atmospheric Administration (NOAA). The model was extended from the original 64 layers to 150 layers to include all the necessary physics in the middle and lower thermosphere as well as electric field and ion-neutral interactions. The WAM simulates neutral wind velocity, neutral temperature, and neutral compositions. WAM employs a spectral hydrostatic dynamical core that integrates a diverse range of atmospheric processes through the common column-physics interface. These processes encompass radiative transfer, hydrological cycle, planetary boundary layer and surface exchange, orographic gravity waves, and vertical eddy mixing. Currently, the WAM operates at a spectral resolution of T62, translating to an approximate grid size of 2° × 2° in latitude and longitude. However, the flexibility of the model allows for convenient adjustments to both horizontal and vertical resolutions if necessary. The WAM has been utilized to study the sudden stratospheric warming (Fuller-Rowell et al., 2010; Pedatella et al., 2016), ionospheric day-to-day variability influence by the lower atmosphere tidal forcing (Fang et al., 2013), and the loss of Starlink satellites due to the enhanced neutral density during a geomagnetic storm (Fang et al., 2022).

The IPE is a time-dependent, three-dimensional, and global model of ionosphere and plasmasphere. It simulates the global distribution of nine ionic species: $O^+$, $H^+$, $He^+$, $N^+$, $NO^+$, ${O_2}^+$, ${N_2}^+$, $O^+$ ($^2D$), and $O^+$ ($^2P$). Additionally, the model calculates the temperatures of electrons and ions, and the plasma drift velocities parallel and perpendicular to the magnetic field lines. The IPE integrated several features including the field line inter-hemispheric plasma (FLIP) model (Richards & Torr, 1996; Richards et al., 2010) as the flux-tube solver and the parallel plasma transport, the global seamless plasma transport perpendicular to the magnetic field, the self-consistent electrodynamic solver (Richmond & Maute, 2013), and the magnetic apex coordinate system (Richmond, 1995) following the full International Geomagnetic Reference Field to enhance its accuracy in studying the global dynamics of the ionosphere and plasmasphere. The flux-tube integrated parameters such as conductivities and wind-driven current are calculated internally in IPE for the electrodynamic solver. The lower boundary of each magnetic flux tube is set to be 90 km. The model is driven by the solar wind interplanetary magnetic field (IMF) parameters and solar $F_{10.7}$ index. The high-latitude potential is defined by Weimer (2005). The nighttime ionization fluxes in this study are adjusted to align with those used in Richmond and Maute (2013) instead of the default values used in FLIP model (Richards et al., 1994). These ionization fluxes are assumed to be constant and do not vary with geographical locations, times of day, seasons, and solar cycles.

The IPE model consists of 80 magnetic longitudes (with a resolution of 4.5°) and 170 flux tubes covering within ±88.12° magnetic latitude. The latitudinal resolution of the model is carefully designed to effectively resolve the dynamic equatorial ionization anomaly feature, with an average resolution of 0.24° equatorward of ±30° magnetic latitude and approximately 1.26° poleward of ±30 magnetic latitude. The count of grid points along a field line, extending from the southern to the northern hemisphere, varies from 11 to 1,115, increasing from the magnetic equator to the highest latitude. Below 150 km altitude, the height distance between every two points in a field line is 2 km. For altitude between 150 and 600 km, the height distance between points increases to 10 km, and for altitude from 600 to 3,000 km, it further extends to 20 km. The IPE model has been used to investigate the Southern Hemisphere Midlatitude Summer Nighttime Anomaly/Weddell Sea Anomaly (Sun et al., 2015), the midlatitude ionospheric peak density structure (N. Maruyama et al., 2016), and the magnetic storm-time response of the ionosphere-plasmasphere coupling (Obana et al., 2019).

The WAM-IPE currently adopts one-way coupled scheme where the neutral atmosphere fields of WAM are systematically remapped to IPE's magnetic grid at each coupling step, with no feedback of IPE parameters into WAM. Operationalized by the National Oceanic and Atmospheric Administration Space Weather Prediction Center (NOAA/SWPC) in July 2021, this coupled model is capable of forecasting the thermosphere and ionosphere conditions 2-days in advance utilizing the space weather drivers forecasted by SWPC.

In this study, the WAM-IPE free run simulations are conducted to examine the longitudinal distribution diurnal variation of the R-T growth rates and their response to PRE during March equinox under conditions of moderate solar activity ($F_{10.7} = 120$ solar flux units [sfu], where 1 sfu equals $10{-}22\ \mathrm{W \cdot m^{-2} \cdot Hz^{-1}}$) and geomagnetic quiet ($Kp = 1$). In addition, WAM-IPE simulations in March under the low ($F_{10.7} = 70$ sfu), moderate ($F_{10.7} = 150$ sfu) and high ($F_{10.7} = 200$ sfu) solar activity levels with fixed geomagnetic activity ($Kp = 1$) were conducted to assess the impact of solar activity on growth rates. For reproducing the seasonal and longitudinal variations of growth rates, WAM-IPE simulations driven by the observed IMF parameters in 5-min cadence are also performed.

## 3. Expression for Rayleigh-Taylor Instability

### 3.1. Modified Apex Coordinates

The base vectors, $\vec{d_i}$ and $\vec{e_i}$, defined in Richmond (1995) are used to derive the new expression of R-T instability growth rate. These vectors are used to define the directions for solving the electrodynamic equations following the definition of modified Apex coordinates. These based vectors, as originally defined in Richmond (1995), are reiterated below for clarity,

$$\overrightarrow{\boldsymbol{d_1}} = (R_E + h_R)\cos\lambda_m \nabla\phi_m \tag{1}$$

$$\overrightarrow{\boldsymbol{d_2}} = -(R_E + h_R)\sin I_m \nabla\lambda_m \tag{2}$$

$$\overrightarrow{\boldsymbol{d_3}} = \frac{\overrightarrow{\boldsymbol{d_1}} \times \overrightarrow{\boldsymbol{d_2}}}{\left\| \overrightarrow{\boldsymbol{d_1}} \times \overrightarrow{\boldsymbol{d_2}} \right\|^2} \tag{3}$$

$$\overrightarrow{\boldsymbol{e_1}} = \overrightarrow{\boldsymbol{d_2}} \times \overrightarrow{\boldsymbol{d_3}} \tag{4}$$

$$\overrightarrow{\boldsymbol{e_2}} = \overrightarrow{\boldsymbol{d_3}} \times \overrightarrow{\boldsymbol{d_1}} \tag{5}$$

$$\overrightarrow{\boldsymbol{e_3}} = \overrightarrow{\boldsymbol{d_1}} \times \overrightarrow{\boldsymbol{d_2}} \tag{6}$$

$$\sin I_m = 2\sin\lambda_m\left(4 - 3\cos^2\lambda_m\right)^{-\frac{1}{2}} \tag{7}$$

where $R_E$ is the mean radius of the Earth, $h_R$ is the 90 km reference height at the base of the dynamo region, $\lambda_m$ is modified magnetic apex latitude, $\phi_m$ is modified magnetic apex longitude, and $I_m$ can be recognized as the equation for the magnetic field inclination in a dipolar geomagnetic field at the radius $R_E + h_R$, but not at other altitudes. Generally, for these base vectors, $\overrightarrow{\boldsymbol{d_1}}$ and $\overrightarrow{\boldsymbol{e_1}}$ point toward the magnetic eastward direction, $\overrightarrow{\boldsymbol{d_2}}$ and $\overrightarrow{\boldsymbol{e_2}}$ are downward/equatorward, and $\overrightarrow{\boldsymbol{d_3}}$ and $\overrightarrow{\boldsymbol{e_3}}$ are parallel to the magnetic field lines. The two sets of the base vectors satisfy the Kronecker delta condition ($\overrightarrow{\boldsymbol{d_i}} \cdot \overrightarrow{\boldsymbol{e_j}} = \delta_{ij}$), but the base vector sets are generally not mutually orthogonal or unit length, unless they lie on a sphere where $R = R_E + h_R$ and the magnetic field is a dipole. While $\overrightarrow{\boldsymbol{d_3}}$ and $\overrightarrow{\boldsymbol{e_3}}$ are parallel, $\overrightarrow{\boldsymbol{e_1}}$ and $\overrightarrow{\boldsymbol{e_2}}$ are in general not aligned with $\overrightarrow{\boldsymbol{d_1}}$ and $\overrightarrow{\boldsymbol{d_2}}$, respectively.

The electrodynamic calculations can be described using either set of the base vectors. In specific scenarios, selecting a particular decomposition yields favorable mapping properties for these components. Richmond (1995) proposed a practical strategy of projecting the electric field ($\overrightarrow{\boldsymbol{E}}$) through the base vectors $\overrightarrow{\boldsymbol{d_i}}$, and expanding the $\frac{\overrightarrow{\boldsymbol{E}}\times\overrightarrow{\boldsymbol{B}}}{B^2}$ velocity as well as the main geomagnetic field ($\boldsymbol{B}_0$) using the base vectors $\overrightarrow{\boldsymbol{e_i}}$. The decomposition, as originally detailed by Richmond (1995), is as follows,

$$\overrightarrow{\boldsymbol{B_0}} = B_{e3}\overrightarrow{\boldsymbol{e_3}} \tag{8}$$

$$\frac{\overrightarrow{\boldsymbol{E}} \times \overrightarrow{\boldsymbol{B_0}}}{{B_0}^2} = v_{e_1}\overrightarrow{\boldsymbol{e_1}} + v_{e_2}\overrightarrow{\boldsymbol{e_2}} = \frac{E_{d_2}}{B_{e_3}}\overrightarrow{\boldsymbol{e_1}} - \frac{E_{d_1}}{B_{e_3}}\overrightarrow{\boldsymbol{e_2}} \tag{9}$$

where $\boldsymbol{E}$ is the negative gradient of an electrostatic potential $\phi$ and $v_{e_1}$ and $v_{e_2}$ are scaled eastward and downward/equatorward velocities. The magnitude can be understood as the drift at the radius $R_E + h_R$ in a dipole field and related to $E_{d_1}$, $E_{d_2}$, and $B_{e_3}$.

Assuming equipotential magnetic field lines, specific factors that influence ionospheric electrodynamics at low and middle latitudes can be studied using a two-dimensional approach (e.g., Haerendel et al., 1992; Richmond, 1995; Richmond et al., 2015). Thus, the Cartesian-like coordinates ($x$, $y$) further defined by Richmond et al. (2015) are applied to simplify some quantities in our following developments. The coordinates $x$ and $y$ are constant along geomagnetic field lines. The coordinate $x$ is proportional to Magnetic Apex longitude, with the proportionality factor being $R = R_E + h_R$. In the equatorial ionosphere, $x$ is approximately magnetic eastward horizontal distance (referenced to 0° magnetic longitude) and $y$ is nearly equal to the apex height. Their derivatives can be described as

$$\nabla x = \nabla(R\phi_m) = \frac{\overrightarrow{\boldsymbol{d_1}}}{\cos\lambda_m} \tag{10}$$

$$\nabla y = \frac{R\sin I_m}{\cos\lambda_m}\nabla\lambda_m = -\frac{\overrightarrow{\boldsymbol{d_2}}}{\cos\lambda_m} \tag{11}$$

### 3.2. Field-Line Integrated Rayleigh-Taylor Instability Growth Rate

The fundamental equations that govern the electrodynamics of the equatorial ionosphere and allow for the derivation of the R-T instability are based on the ion continuity equation and the ionospheric dynamo equations. After decomposing the transport term into perpendicular and parallel components, we can rewrite the continuity equation in the $F$ region as follows:

$$\frac{\partial n}{\partial t} + \nabla\cdot\left(\frac{n}{B^2}\overrightarrow{\boldsymbol{E}}\times\overrightarrow{\boldsymbol{B}}\right) + \nabla\cdot\left(n\overrightarrow{\boldsymbol{v}_{\parallel}}\right) = q - l \tag{12}$$

where $n$ is the plasma density, $\overrightarrow{\boldsymbol{v}_{\parallel}}$ is the plasma drift parallel to magnetic field lines, $q$ is the production term, and $l$ is the loss term. The second and third terms on the left-hand side represent the divergence of plasma flux due to transport, which signifies the corresponding rate of loss per unit volume and unit time. This equation is only valid in the $F$ region since ions do not drift at $\frac{\overrightarrow{\boldsymbol{E}}\times\overrightarrow{\boldsymbol{B}}}{B^2}$ velocity in the $E$ region. In the ionosphere, the magnetic field can be written as $\overrightarrow{\boldsymbol{B}} = \overrightarrow{\boldsymbol{B_0}} + \overrightarrow{\boldsymbol{\delta B}}$, representing the total magnetic field that encompasses both the Earth's main field ($\overrightarrow{\boldsymbol{B_0}}$) and the perturbation field ($\overrightarrow{\boldsymbol{\delta B}}$) induced by electric currents. However, due to the significantly smaller magnitude of $\overrightarrow{\boldsymbol{\delta B}}$ compared to $\overrightarrow{\boldsymbol{B_0}}$, it is reasonable to neglect the contribution of $\overrightarrow{\boldsymbol{\delta B}}$. Similarly to the electric field derived from the scalar electric potential $\phi$, the main component $\overrightarrow{\boldsymbol{B_0}}$ can be formulated as the negative gradient of a scalar magnetic potential $\psi$ (e.g., Gauss, 1838; Glassmeier & Tsurutani, 2014). Therefore, the divergence of the cross product of electric field and magnetic field is,

$$\nabla\cdot\left(\overrightarrow{\boldsymbol{E}}\times\overrightarrow{\boldsymbol{B}}\right) = \nabla\cdot(\nabla\phi\times\nabla\psi) = 0 \tag{13}$$

and the continuity equation can be written as,

$$\frac{\partial}{\partial t}\left(\frac{n}{B^2}\right) + \frac{\overrightarrow{\boldsymbol{E}}\times\overrightarrow{\boldsymbol{B}}}{B^2}\cdot\nabla\left(\frac{n}{B^2}\right) + \frac{1}{B^2}\nabla\cdot\left(n\overrightarrow{\boldsymbol{v}_{\parallel}}\right) = \frac{q-l}{B^2} \tag{14}$$

in which the second and third terms are associated with transport perpendicular and parallel to $\overrightarrow{\boldsymbol{B}}$, respectively. Some of these terms can be decomposed and simplified for mapping to the magnetic field lines and expressed as,

$$\nabla\left(\frac{n}{B^2}\right) = \frac{\partial}{\partial x}\left(\frac{n}{B^2}\right)\nabla x + \frac{\partial}{\partial y}\left(\frac{n}{B^2}\right)\nabla y \tag{15}$$

$$\nabla\cdot\left(n\overrightarrow{\boldsymbol{v}_{\parallel}}\right) = \nabla\cdot\left(\frac{nv_{\parallel}}{B}\overrightarrow{\boldsymbol{B}}\right) = \overrightarrow{\boldsymbol{B}}\cdot\nabla\left(\frac{nv_{\parallel}}{B}\right) + \frac{nv_{\parallel}}{B}\nabla\cdot\overrightarrow{\boldsymbol{B}} = B\frac{\partial}{\partial s}\left(\frac{nv_{\parallel}}{B}\right) \tag{16}$$

where $s$ is the distance along field lines. $\nabla\cdot\overrightarrow{\boldsymbol{B}}$ is zero based on Gauss's law. Substituting Equations 10, 11, 15, and 16 into Equation 14 and applying $\overrightarrow{\boldsymbol{d_i}}\cdot\overrightarrow{\boldsymbol{e_j}} = \delta_{ij}$ to $\overrightarrow{\boldsymbol{E}}\times\overrightarrow{\boldsymbol{B}}$ yields the continuity equation in Modified Magnetic Apex coordinates as,

$$\frac{\partial}{\partial t}\left(\frac{n}{B^2}\right) + \frac{v_{e1}}{\cos\lambda_m}\frac{\partial}{\partial x}\left(\frac{n}{B^2}\right) - \frac{v_{e2}}{\cos\lambda_m}\frac{\partial}{\partial y}\left(\frac{n}{B^2}\right) + \frac{1}{B}\frac{\partial}{\partial s}\left(\frac{nv_{\parallel}}{B}\right) = \frac{q-l}{B^2} \tag{17}$$

Let us define some quantities,

$$\nabla z = -\nabla V = \vec{\boldsymbol{B}} \tag{18}$$

$$\frac{\mathrm{d}z}{ds} = B \tag{19}$$

where $z = -V$, orthogonal to $x$ and $y$. By applying this definition, it is convenient to integrate Equation 17 with respect to $z$ through the $F$ region with a lower boundary at 150 km. Note that owing to the considerable reduction of ion density in the $E$ region during nighttime, the density can be considered negligible below 150 km. Furthermore, it is established that $v_{e1}$, $v_{e2}$, and $\cos\lambda_m$ are independent of $z$. These allow the field line integral to be expressed in the following form.

$$\begin{gathered}\frac{\partial}{\partial t}\int_{S(150)}^{N(150)}\frac{n}{B}\frac{dz}{B}+\frac{v_{e1}}{\cos\lambda_m}\frac{\partial}{\partial x}\int_{S(150)}^{N(150)}\frac{n}{B}\frac{dz}{B}-\frac{v_{e2}}{\cos\lambda_m}\frac{\partial}{\partial y}\int_{S(150)}^{N(150)}\frac{n}{B}\frac{dz}{B}+\\ \int_{S(150)}^{N(150)}\frac{\partial}{\partial s}\left(\frac{nv_{\parallel}}{B}\right)\frac{dz}{B}=\int_{S(150)}^{N(150)}\frac{q-l}{B}\frac{dz}{B}\end{gathered} \tag{20}$$

where the parallel transport term $\int_{S(150)}^{N(150)}\frac{\partial}{\partial s}\left(\frac{n\boldsymbol{v}_{\parallel}}{B}\right)\frac{dz}{B}$ represents the net flux of ions out of the ends of flux tubes at 150 km altitude. Considering our assumption that $n$ equals zero at 150 km, this term should consequently be set to zero. This enables us to conveniently simplify the entire equation using the following new quantity.

$$\int_{S(150)}^{N(150)}\frac{n}{B}\frac{dz}{B}=\int_{S(150)}^{N(150)}\frac{n}{B}ds=\eta \tag{21}$$

where $\eta$ represents ions per unit magnetic flux. In the nighttime ionosphere, the production term can be neglected in the $F$ region, while the loss term, associated with the recombination rate, is significant in the $E$ and the lower $F$ regions (Sultan, 1996). Although the lower boundary is set at 150 km to exclude the effects from the $E$ region, the recombination rate in the lower $F$ region still influences the calculation of the growth rate. To maximize the R-T growth rate, the loss term is neglected. By substituting Equation 21 into Equation 20, the integral becomes,

$$\frac{\partial\eta}{\partial t}+\frac{v_{e1}}{\cos\lambda_m}\frac{\partial\eta}{\partial x}-\frac{v_{e2}}{\cos\lambda_m}\frac{\partial\eta}{\partial y}=0 \tag{22}$$

This nonlinear equation is appropriate for understanding the time evolution of instability. However, to investigate whether a specific area in the ionosphere is susceptible to instability, calculating magnetic flux tube integrated linear growth rate allows us to determine the stability of the ionospheric conditions. With subscript zero denoting unperturbed quantities and primes denoting perturbations, the linearization of Equation 22 can take on the following expression,

$$\begin{gathered}\frac{\partial\eta_0}{\partial t}+\frac{v_{e1_0}}{\cos\lambda_m}\frac{\partial\eta_0}{\partial x}-\frac{v_{e2_0}}{\cos\lambda_m}\frac{\partial\eta_0}{\partial y}\\ +\frac{\partial\eta'}{\partial t}+\frac{v_{e1_0}}{\cos\lambda_m}\frac{\partial\eta'}{\partial x}-\frac{v_{e2_0}}{\cos\lambda_m}\frac{\partial\eta'}{\partial y}+\frac{v_{e1}'}{\cos\lambda_m}\frac{\partial\eta_0}{\partial x}-\frac{v_{e2}'}{\cos\lambda_m}\frac{\partial\eta_0}{\partial y}=0\end{gathered} \tag{23}$$

In this expression the sum of the first three (zero-order) terms representing the background or steady-state condition is assumed to be zero. The next three terms involving derivatives of $\eta'$ represent the convective derivative of $\eta'$, $\frac{D\eta'}{Dt}$, which is the rate of change of $\eta'$ in a reference frame moving in the $x$ and $y$ directions with background velocity components $\frac{v_{e1_0}}{\cos\lambda_m}$ and $-\frac{v_{e2_0}}{\cos\lambda_m}$, respectively. As in many earlier calculations of the R-T instability (Ossakow, 1981; Sultan, 1996; Zalesak & Ossakow, 1982), we analyze perturbations that have much shorter spatial scales in the east-west direction than in the vertical/meridional direction. The perturbation electric field is then predominantly zonal (since the gradient of the perturbation electric potential is predominantly zonal), and the $\vec{\boldsymbol{E}} \times \vec{\boldsymbol{B}}$ velocity is predominantly vertical/meridional. That is, $v'_{e1}$ can be neglected in comparison with $v'_{e2}$. Consequently, the linear continuity equation becomes,

$$\frac{D\eta'}{Dt} - \frac{v'_{e2}}{\cos\lambda_m}\frac{\partial\eta_0}{\partial y} = 0 \tag{24}$$

The first-order vertical drift velocity is as follows,

$$v'_{e2} = -\frac{E'_{d1}}{B_{e3}} = -\frac{E'_x}{B_{e3}\cos\lambda_m} \tag{25}$$

where $E'_x$ represents perturbation electric field. To study whether and how fast the perturbation is growing, it is essential to establish the relationship between $\eta'$ and $v'_{e2}$. Therefore, we applied the integrated Ohm's Law expression in $x$ direction, Equation A5 in Richmond et al. (2015), to determine $E'_x$. Under the assumption of equipotential geomagnetic field lines, the equation is described as follows,

$$K_x = \Sigma_x E_x + (\Sigma_H - \Sigma_c) E_y + K_x^D \tag{26}$$

where $\Sigma_x$ represents the Pedersen conductance in the $x$ direction while $\Sigma_H$ denotes the Hall conductance. The presence of $\Sigma_c$, dependent on Pedersen conductance, is attributed to the nonorthogonality of $\overrightarrow{\boldsymbol{d_1}}$ and $\overrightarrow{\boldsymbol{d_2}}$ in a realistic geomagnetic field. The integral can be expressed as,

$$\Sigma_c = \int_S^N \frac{\sigma_p \overrightarrow{\boldsymbol{d_1}} \cdot \overrightarrow{\boldsymbol{d_2}}}{D} ds \tag{27}$$

where $D$ is magnetic field distortion, and it is defined as $D \equiv \left| \overrightarrow{\boldsymbol{d_1}} \times \overrightarrow{\boldsymbol{d_2}} \right|$ (Richmond, 1995). Additionally, $K_x$ encompasses the field-line-integrated current density and $K_x^D$ is the field-line-integrated dynamo current density, which includes both wind-driven and gravity-driven current densities and can be written as,

$$K_x^D = B_{e_3}\cos\lambda_m \int_S^N \left[ \frac{\sigma_p d_1^2}{D} u_{e_2} + \left( \sigma_H - \frac{\sigma_p \overrightarrow{\boldsymbol{d_1}} \cdot \overrightarrow{\boldsymbol{d_2}}}{D} \right) u_{e_1} + \frac{n m_i \overrightarrow{\boldsymbol{e_2}} \cdot \overrightarrow{\boldsymbol{g}}}{B_{e_3} B} \right] ds \tag{28}$$

Assuming that the zeroth order terms of Equation 23 balance each other, and that the $y$ component of the perturbation electric field can be neglected, the primary perturbation current can be obtained from Equation 26,

$$K'_x = \Sigma_{x_0} E'_x + K_x^{D'} - \Sigma'_c E_{y_0} + \Sigma'_x E_{x_0} + \Sigma'_H E_{y_0} + \Sigma_{H_0} E'_y - \Sigma_{c_0} E'_y = 0 \tag{29}$$

The $E'_y$ and $E'_x$ are corresponding to $v'_{e1}$ and $v'_{e2}$ in Equation 23, it follows that $\Sigma_{H_0} E'_y - \Sigma_{c_0} E'_y$ is negligible. Furthermore, the inclusion of Hall conductance significantly complicates the mathematical analysis, requiring further investigation in future studies. Our focus is on the perturbations in the $F$ region, and for simplicity, we assume that the perturbation of nighttime Hall conductance $\Sigma'_H$ is small enough to be ignored. Since the Hall conductance primarily lies below 150 km altitude (See Figure S1), this assumption means that ion transport is neglected below 150 km, corresponding to the condition of night-time photochemical equilibrium in the $E$ region. As a result, the perturbation electric field in $x$ direction can be written as follows,

$$E'_x = -\frac{K_x'^D}{\Sigma_{x_0}} + \frac{E_{y_0}}{\Sigma_{x_0}} \Sigma'_c - \frac{E_{x_0}}{\Sigma_{x_0}} \Sigma'_x \tag{30}$$

$$K_x'^D = B_{e_3}\cos\lambda_m \int_S^N \left[ \frac{\sigma'_p d_1^2}{D} u_{e_2} + \left( \sigma'_H - \frac{\sigma'_p \overrightarrow{\boldsymbol{d_1}} \cdot \overrightarrow{\boldsymbol{d_2}}}{D} \right) u_{e_1} + \frac{n' m_i \overrightarrow{\boldsymbol{e_2}} \cdot \overrightarrow{\boldsymbol{g}}}{B_{e_3} B} \right] ds \tag{31}$$

The perturbation dynamo current, $K'^{D}_{x}$, mainly varies due to changes in ion density and conductivities. Note that when the perturbation in the $E$ region is involved, $\sigma'_H$ may become significant and cannot be ignore. Substituting Equation 29 into Equation 24 we obtain the following perturbation equation,

$$\frac{D\eta'}{Dt} - \frac{\left(\Sigma'_x E_{x_0} + K'^{D}_{x} - \Sigma'_c E_{y_0}\right)}{\Sigma_{x_0} B_{e3}\cos^2\lambda_m}\frac{\partial \eta_0}{\partial y} = 0 \tag{32}$$

Here, let us make a set of assumptions.

$$\frac{K'^{D}_{x}}{K^{DF}_{x_0}} \cong \frac{\Sigma'_c}{\Sigma^F_{c_0}} \cong \frac{\Sigma'_x}{\Sigma^F_{x_0}} \cong \frac{\eta'}{\eta_0} \tag{33}$$

where $\eta'$ is the perturbation in the flux-tube electron content and where superscripts $F$ indicate that the field-line integrals have a lower boundary of 150 km. We assume that above 150 km the electron density changes by the same fraction at all points along a field line. Since the Pedersen conductivity is proportional to the density, and the Hall conductivity can be neglected in the $F$ region, these assumptions ensure that any variations in $K'^{D}_{x}$ originating from different points along the field line would also change by an identical fraction as the electron density. Similar assumptions are also applied to the relative perturbations in $\eta'$, $\Sigma'_x$ and $\Sigma'_c$. The process of validating the feasibility of Equation 32 can be found in Appendix A. Then, Equation 32 can be written as,

$$\frac{D\eta'}{Dt} - \frac{\left(\Sigma^F_{x_0} E_{x_0} + K^{DF}_{x_0} - \Sigma^F_{c_0} E_{y_0}\right)}{\Sigma_{x_0} B_{e3}\cos^2\lambda_m \eta_0}\frac{\partial \eta_0}{\partial y}\eta' = 0 \tag{34}$$

It should be noted that, in contrast to the quantities marked with superscripts $F$, the lower boundary for $\Sigma_{x_0}$ is 90 km. In the scenario of R-T instability, this linear equation can be utilized to characterize the dynamics of the interface at the steep vertical density gradient region. The coefficient of $\eta'$ has a specific significance—it represents the growth rate or decay rate and determines the rate at which $\eta'$ changes with time. If the coefficient of $\eta'$ is denoted as $\gamma$, the solution of $\eta'$ will vary in time as $Ce^{\gamma t}$, where $C$ is any nonzero constant. This allows us to understand how perturbations of $\eta'$ can grow in time. According to Equations 25 and 30, the direction of $v'_{e2}$ can be defined by the parentheses in Equation 34 multiplied by $\frac{\partial \eta_0}{\partial y}\eta'$. During the evening sector at the bottom side $F$ region, where $\frac{\partial \eta_0}{\partial y}$ takes a positive value, the sum of the three terms in the parentheses must be positive for growing EPBs, where $v'_{e2}$ and $\eta'$ have the same sign. In turn, this causes a bubble perturbation to amplify exponentially and penetrate into denser background plasma.

Since the field line ion content is roughly proportional to the gravity driven current, we can make an assumption that $\frac{1}{\eta_0}\frac{\partial \eta_0}{\partial y}$ is approximately equal to $\frac{1}{K^{gF}_{x_0}}\frac{\partial K^{gF}_{x_0}}{\partial y}$, based on a quantity our model routinely calculates,

$$K^{gF}_{x_0} = \cos\lambda_m \int_{S(150)}^{N(150)} \frac{n_0 m_i \vec{e_2}\cdot\vec{g}}{B} ds \tag{35}$$

This approximation leads to the derivation of the final expression for calculating the growth rate of the R-T instability incorporating the Modified Apex coordinate system as,

$$\gamma = \frac{\left(\Sigma^F_{x_0} E_{x_0} + K^{DF}_{x_0} - \Sigma^F_{c_0} E_{y_0}\right)}{K^{gF}_{x_0}\Sigma_{x_0} B_{e_3}\cos^2\lambda_m}\frac{\partial K^{gF}_{x_0}}{\partial y} \tag{36}$$

## 4. Simulation Results

Using Equation 36, the R-T growth rates derived from the WAM-IPE simulations under various conditions are evaluated. Simulations were conducted for the 20 March under moderate solar activity conditions ($F_{10.7}$ = 120 sfu) and geomagnetic quiet time ($Kp$ = 1), focusing on the longitudinal distribution and diurnal

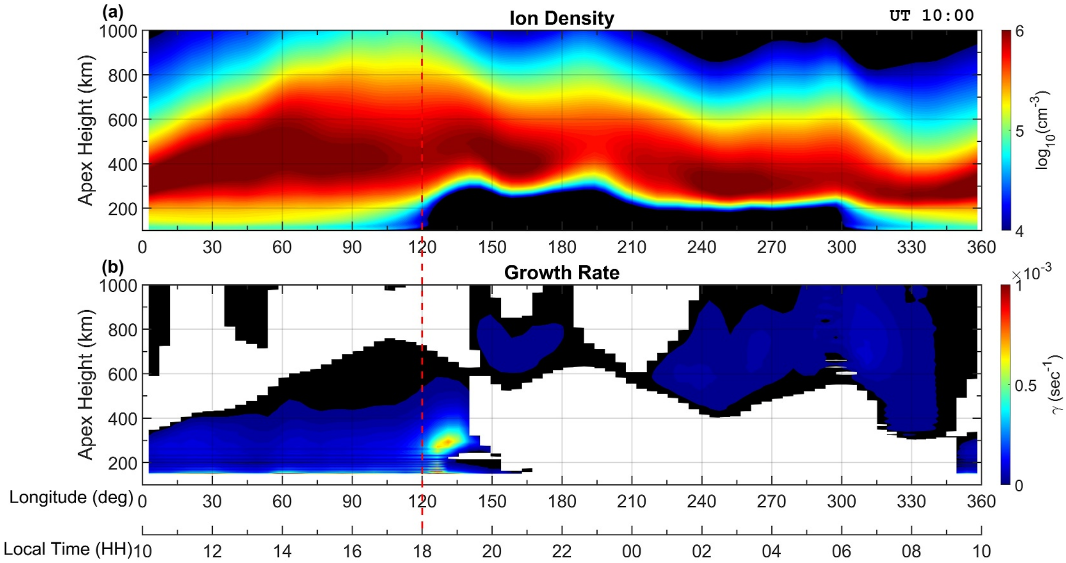

**Figure 1.** Longitudinal distribution of (a) ion density and (b) Rayleigh-Taylor growth rate with apex height at magnetic equator at 1000 UT on 20 March. The vertical red dashed line denotes 1800 LT. The simulation is driven by $F_{10.7}$ of 120 sfu and *Kp* of 1.

variation of the R-T growth rate, as well as its dependence on the PRE (Figures 1–3). The model runs were initiated 3 days before to achieve a diurnally reproduceable condition. Figures 1a and 1b shows the ion density and R-T growth rate in geographic longitude and apex height at 1000 UT. The ion density reveals a clear diurnal variation. During the daytime, higher ion density values can be seen in a wide range of altitudes between 100 and 1,000 km. At nighttime, due to the recombination process in the *E* region, the ion densities rapidly decrease in the bottomside ionosphere. Between longitudes of 120°E and 150°E in the post-sunset sector, a pronounced

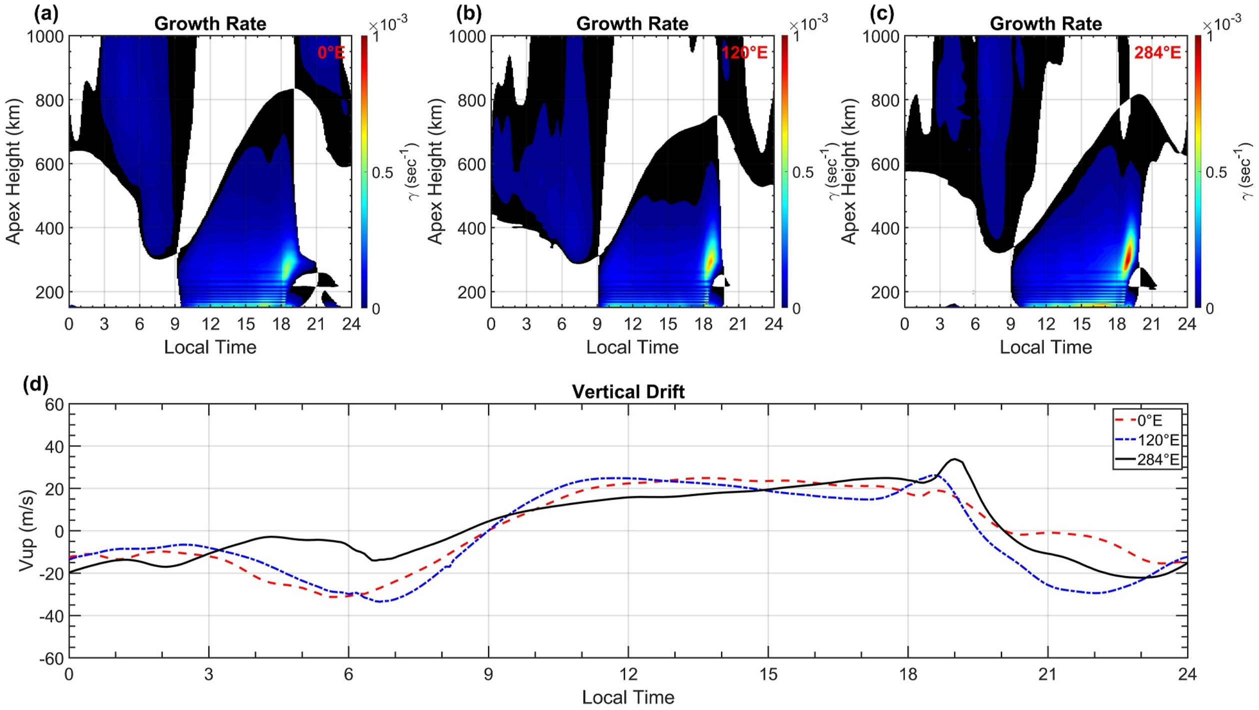

**Figure 2.** Diurnal variations of (a)–(c) Rayleigh-Taylor growth rates and (d) vertical drifts at magnetic equator on 20 March. From left to right is at different longitude of 0, 120, and 284°E, respectively. The simulations are under the same solar and geomagnetic condition as in Figure 1.

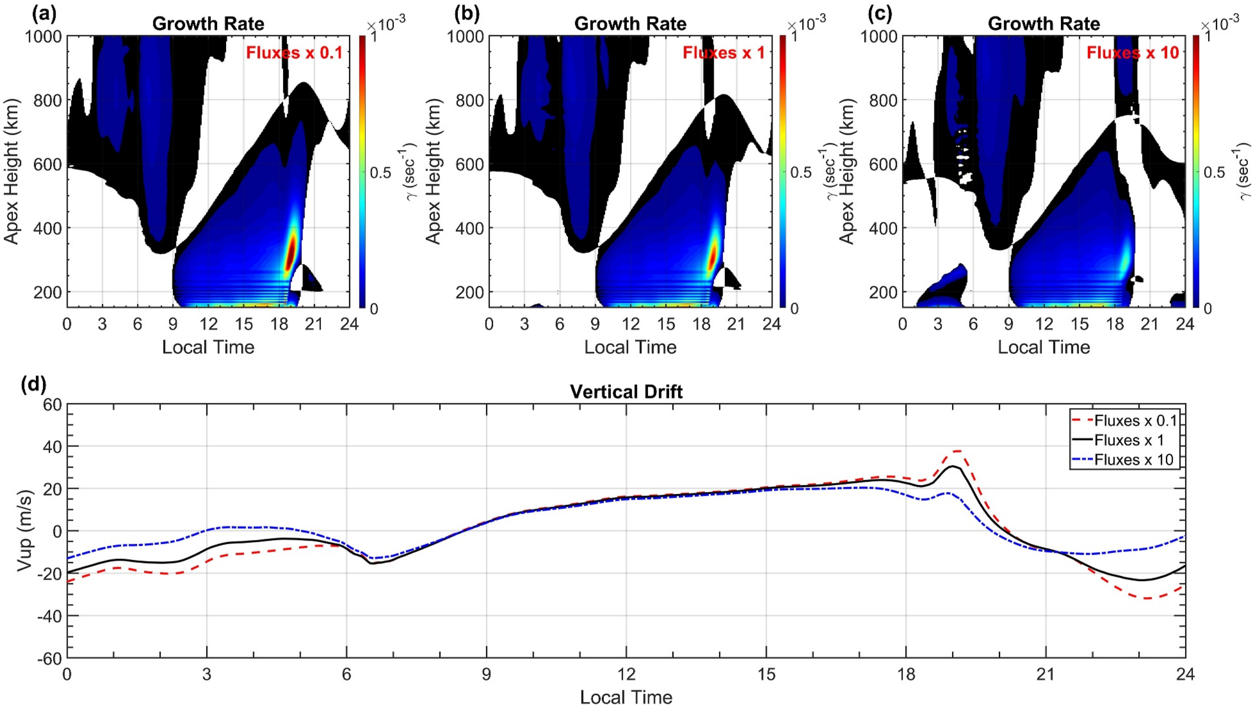

**Figure 3.** The Rayleigh-Taylor growth rate (a–c) and the vertical drift (d) at 284°E response to different Pre-reversal enhancements on 20 March. The three columns in the top panel and the three differently colored lines in the bottom panel represent the cases of nighttime fluxes multiplied by factor of 0.1, 1, and 10, respectively. The $F_{10.7}$ and the $Kp$ are same as those in Figure 1.

upwelling structure is observed, which results from the upward vertical drift associated with the PRE. Notably, the maximum growth rate is observed just beneath the upwelling structure, spanning longitudes from 120°E to 130°E with peak magnitudes occurring between altitudes of 200 and 300 km. The maximum magnitude of the growth rate is $7.2 \times 10^{-4}\ \mathrm{s}^{-1}$ corresponding to a growth time of approximately 23.1 min. This growth rate is slower than the rates reported in Huba (2022) and Wu (2015), but comparable to the rate shown in Sultan (1996). Note that the appearance of the horizontal stripes below 250 km is caused by the grid design of IPE. The points along the field lines are not evenly distributed, leading to the artificial patterns when calculating $\frac{\partial K_{x_0}^{gF}}{\partial y}$ in Equation 36. However, these small perturbations caused by the uneven grid design are not sufficient to affect the large plasma density gradient in the bottomside $F$ region during the post-sunset sector. In order to avoid the influences from the artificial patterns, following analyses will focus on the field lines with apex heights above 250 km.

Figures 2a–2d demonstrate the diurnal variation of growth rates and equatorial vertical $\vec{E} \times \vec{B}$ drifts at 300 km at three different longitudes under the same simulation conditions as those in Figure 1. Pronounced growth rates are observed between altitudes of 250 and 400 km, occurring near dusk at 1800~2000 local time (LT) for all three longitudes. The occurrence times of these strong growth rates match precisely with the timing of PRE in each longitude region. This is because the first term in parentheses in Equation 36, proportional to $E_{x_0}$, dominates over the other two terms, which include the gravity effect. Comparing the three locations, the growth rate and the upward drift are stronger at the longitude of 284°E (Figures 2c and 2d). In addition, the values and altitude distribution of the growth rate show a positive correlation with the upward drift.

To further validate our equation for the R-T growth rate, controlled experiments on the magnitude of the PRE are carried out. The PRE drift magnitude is changed by multiplying the standard nighttime ionization rates by a factor of 0.1 or 10 (Fesen et al., 2000). Similar numerical experiments have been previously carried out by Richmond and Fang (2015). Since the model $E$-region ion density is in photochemical equilibrium where dissociative recombination dominates, the nighttime $E$ region ion densities and conductivities should be effectively reduced by roughly 0.32 with the 0.1 multiplication factor ($\sqrt{0.1} = 0.32$) and increased by roughly 3.2 times with the 10 multiplication factor ($\sqrt{10} = 3.2$) compared to the standard case. These modifications also have an impact on the

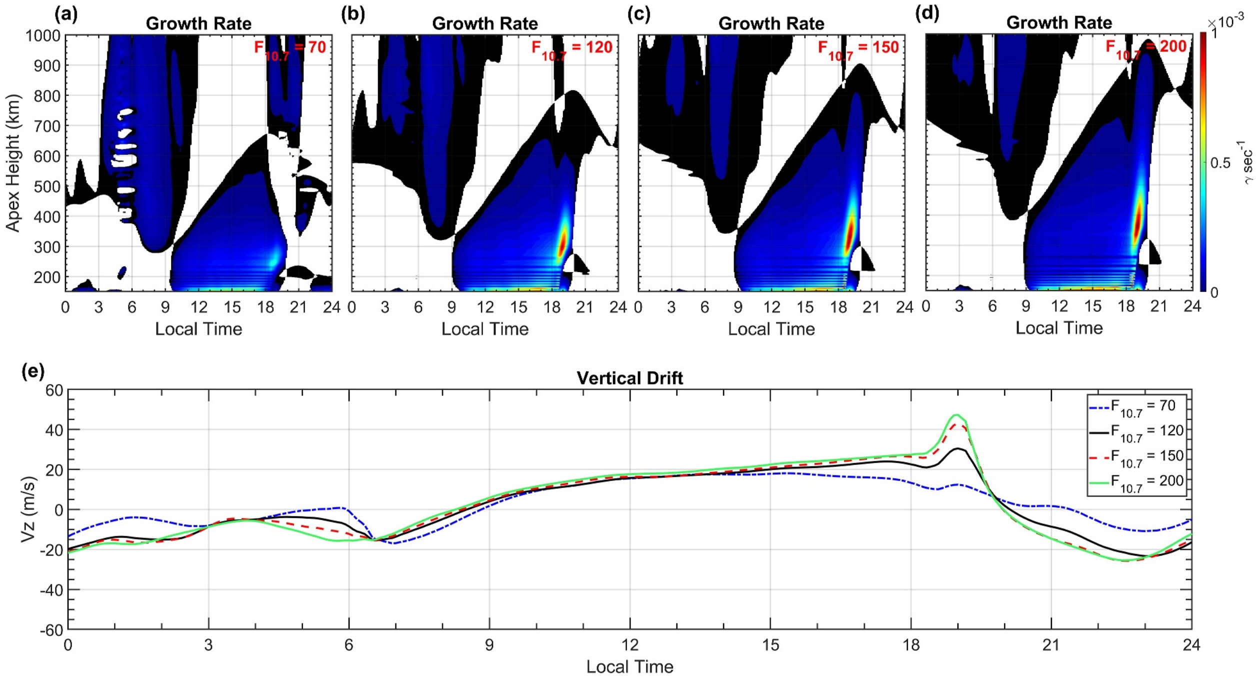

**Figure 4.** The Rayleigh-Taylor growth rate (a–d) and the vertical drift (e) at 284°E response to different solar activities on 20 March. The simulations, conducted during a magnetic quiet time with a $Kp$ value of 1, are driven by four different $F_{10.7}$ levels of 70, 120, 150, and 200 sfu, respectively.

$F$ region conductivity, as they influence the vertical plasma drift during nighttime. Figures 3a–3d illustrate the responses of the growth rate and vertical drifts to different settings of nighttime ionization rates at 284°E. Note that Figure 3b and the black line in Figure 3d are the same as Figure 2c and the black line in Figure 2d, acting as a base case for comparison with cases involving increased and decreased nighttime fluxes. The results show that a decrease (increase) in nighttime ionization results in a stronger (weaker) upward drift during the PRE. In Figures 3a–3c the maximum growth rate reaches approximately $1.2 \times 10^{-3}$ s$^{-1}$, $9.5 \times 10^{-4}$ s$^{-1}$, and $5.0 \times 10^{-4}$ s$^{-1}$, and in Figure 3d the associated PRE vertical drift peaks at 37, 30, and 17 m/s. Furthermore, the growth rates extend to higher apex heights and strengthen in Figure 3a, whereas they decrease in altitude and magnitude in Figure 3c. This demonstrates that our growth rates derived from these simulations respond reasonably to different magnitudes of the PRE vertical drifts, which are consistent with previous studies (e.g., Jayachandran et al., 1993; Kil et al., 2009; Wu, 2017).

Figures 4a–4e show the results of growth rates and vertical drifts at 284°E under four different solar activity conditions, characterized by $F_{10.7}$ indices of 70, 120, 150, and 200 sfu during geomagnetic quiet times ($Kp = 1$). Note that the model nighttime ionization rate does not depend on $F_{10.7}$, although in reality there may be a complex dependence due to scattering of variable sunlight from the variable geocoronal hydrogen. The results show that stronger solar activity will produce greater vertical drift near the PRE, which in turn increases growth rates below 400 km and raises the occurrence of positive growth rates at higher altitudes. However, the maximum values of the growth rate under these four different solar activity conditions (from low to high) are $4.2 \times 10^{-4}$ s$^{-1}$, $9.5 \times 10^{-4}$ s$^{-1}$, $1.0 \times 10^{-3}$ s$^{-1}$, and $1.0 \times 10^{-3}$ s$^{-1}$, respectively, indicating that they do not exhibit a perfect linear relation with solar activity when they reach a certain level. In fact, the experiments in Figures 3 and 4 are similar because the strength of the PRE is directly related to solar activity. This saturation feature in growth rates during high solar activities indicates that while vertical drift is one of the main factors, other factors can also impact the variations of the R-T growth rate such as solar variation induced changes in photoionization and the evening zonal convection (Richmond et al., 2015) in the ionosphere, which will be investigated in a future study.

Our analyses based on Figures 1–4 demonstrate that the new R-T growth rate calculation reproduces reasonable spatial and LT distributions, as well as solar activity variations, which are consistent with previously established knowledge. Thus, we further expand the study to cover the entire year of 2013 to investigate the seasonal variability of the growth rates and the vertical ion drift. In this annual run, the 5-min observed solar and

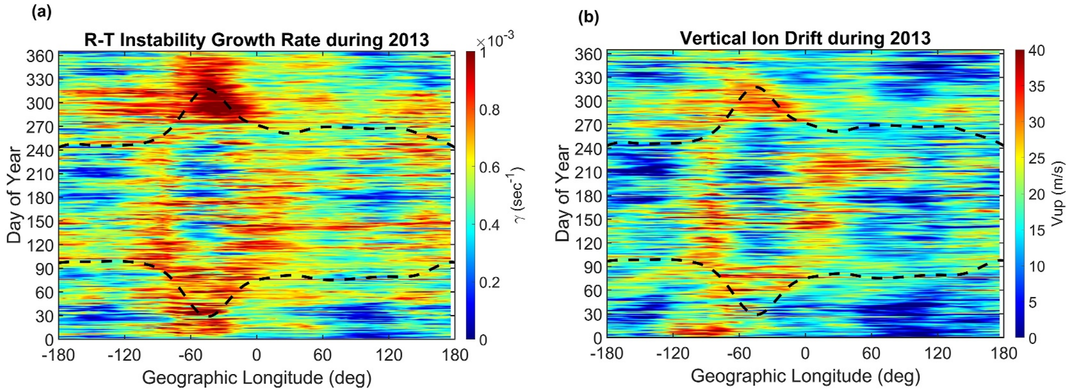

**Figure 5.** Seasonal and longitudinal variations of (a) Rayleigh-Taylor growth rate and (b) vertical ion drift during 2013 driven by observed solar and interplanetary parameters. The dashed lines represent the days when the solar terminator aligns with the magnetic field line.

interplanetary parameters are used to drive the WAM-IPE. Figure 5a shows the seasonal and longitudinal variation of the R-T growth rates. Each value in this plot is calculated based on the maximum values between 200 and 400 km altitude and within the LT range of 18–20 LT. Superimposed black dashed lines mark the days when the solar terminator aligns with the magnetic field line. The most significant growth rates are predominantly observed in the longitude range spanning from 90°W to 60°E during the periods of day 0–90 (from January to March) and day 270–330 (from September to November). Meanwhile, moderate growth rates are distributed across longitude regions extending from 90°W to 30°E during day 90–150 and day 210–240 (corresponding to April, May, and August), as well as from 30°W to 30°E during day 330–365 (in December), with additional occurrences around other longitudes near the equinox seasons. The growth rates during the two solstice seasons are notably lower compared to other seasons globally, particularly around the June solstice (day 172). As for the vertical ion drift depicted in Figure 5b, the maximum values are picked at 300 km altitude within the LT range of 18–20 LT. The morphologies of the vertical ion drift closely resemble those of the R-T growth rates. It is worth noting that the magnitude of the growth rate appears to have different responses to the magnitude of the vertical ion drift at different longitudes. Nevertheless, the characteristics of the vertical ion drift distribution coincide with those of the growth rate distribution.

In general, the growth rate distributions agree with Tsunoda (1985) that EPBs occurrences peak when the terminator is aligned with the Earth's magnetic field. The overall pattern of growth rate closely corresponds to the bubble occurrence and the scintillation maps detected through satellite observations at various altitudes (e.g., Gentile et al., 2006; C. S. Huang et al., 2014; C. Y. Huang et al., 2022). While there are some discrepancies in some regions, such as the longitude of 90°W during June solstice and the longitude region between 120°W and 180°W around September equinox, the general trend indicates a strong correlation between the growth rate and the prior satellites observations of irregularities. This result suggests the new R-T growth rate calculation with WAM-IPE reasonably reproduces the climatology and has high potential for integration into operational WAM-IPE to explore the feasibility of EPB monitoring and even forecasting.

## 5. Discussion

The estimation of the linear R-T growth rate has been discussed in various studies in past decades. One of the most well-known and commonly applied expression is the equation proposed by Sultan (1996), which is as follows:

$$\gamma = \frac{\Sigma^F_{P,0}}{\Sigma^E_{P,0} + \Sigma^F_{P,0}}\left(V_p - U^P_L - \frac{g_e}{\nu^F_{\mathrm{eff}}}\right)K^F - R_T \tag{37}$$

where $\Sigma^F_{P,0}$ and $\Sigma^E_{P,0}$ are field line integrated $F$ (starting at 200 km) and $E$ region (starting at 125 km) Pedersen conductivities, $V_p$ is the flux-tube integrated plasma velocity perpendicular to the magnetic field associated with the zonal electric field, $U^P_L$ is the flux-tube integrated neutral wind weighted by Pedersen conductivity in the meridional/vertical direction, $g_e$ and $\nu^F_{\mathrm{eff}}$ are the effective gravity (positive upward) and the effective $F$-region collision frequency weighted by the flux-tube plasma density, $K^F$ is the height gradient of the $F$-region flux tube electron content, and $R_T$ is the flux-tube mean dissociative recombination loss rate. This Equation utilizes the flux-tube coordinate $L$ (McIlwain, 1961) and longitude angle $\phi$. Further details can be found in Haerendel et al. (1992) and Sultan (1996). In comparison to Equation 37, Equation 36 in our paper shows a strong similarity, as both pertain to a horizontally uniform background state. The specific similarities are marked as follows,

$$\frac{\Sigma^F_{x_0} E_{x_0}}{\Sigma_{x_0} B_{e_3} \cos^2\lambda_m} \sim \frac{\Sigma^F_{P,0}}{\Sigma^E_{P,0} + \Sigma^F_{P,0}} V_p$$

$$\frac{K^{DF}_{x_0}}{\Sigma_{x_0} B_{e_3} \cos^2\lambda_m} \sim \frac{\Sigma^F_{P,0}}{\Sigma^E_{P,0} + \Sigma^F_{P,0}} \left( -U^P_L - \frac{g_e}{\nu^F_{\mathrm{eff}}} \right)$$

$$\frac{\partial K^{gF}_{x_0}}{K^{gF}_{x_0} \partial y} \sim K^F$$

Note that the $K^{gF}_{x_0}$ in the denominator arises from the assumption in Equation 35 and the entire expression $\frac{\partial K^{gF}_{x_0}}{K^{gF}_{x_0} \partial y}$ represents the gradient scale length. While Equations 36 and 37 are quite similar, they have some fundamental differences due to their different assumptions. The primary advantage of our R-T growth rate expression and the key distinction between Equations 36 and 37 lies in the usage of Quasi-Dipole coordinates, which allows for a more precise representation of geomagnetic field influences on the plasma dynamics (Richmond, 1995). This results in the electrodynamics equations differ from those in the dipole coordinate system.

Our use of a realistic geomagnetic-field geometry introduced terms involving $\frac{\sigma_p \overrightarrow{\boldsymbol{d_1}} \cdot \overrightarrow{\boldsymbol{d_2}}}{D}$ in Equations 30 and 31, terms that are non-zero when the non-orthogonality of Magnetic Apex coordinates is taken into account. At low latitudes these terms are usually small and change sign with respect to longitude, maximizing or minimizing over South America, the Atlantic Ocean, and Africa. Because $\overrightarrow{\boldsymbol{d_1}} \cdot \overrightarrow{\boldsymbol{d_2}}$ usually changes sign with respect to latitude near the magnetic equator, these terms will be most important when there is a strong north-south asymmetry of the Pedersen conductivity and zonal wind across the magnetic equator, because this asymmetry would be multiplied by the asymmetry of $\overrightarrow{\boldsymbol{d_1}} \cdot \overrightarrow{\boldsymbol{d_2}}$ when the field-line integrals are computed along the entire field line. Since the terms are usually small, we have not attempted to quantify them in detail in this study.

Another point of the distinction in the dynamo term lies in the gravity-driven current utilization. The approximation of $F$-region Pedersen conductivity can be written as $nm_i\nu_{in}/B^2$. If this expression for the Pedersen conductivity is substituted into Equation 37, it can yield the gravity-driven current as depicted in Equation 35. This simplification omitted the calculation of the effective collision frequency, making the overall calculation more convenient.

In addition, the effect of recombination rate on the growth rate is not considered in this study. Bittencourt and Abdu (1981) proposed that recombination effects become negligible when production is absent and the $h'F$ is near or above 300 km. Sultan (1996) also suggests that the recombination effects are important in the $E$ and lower $F$ regions, which would suppress the R-T growth rate. The boundary of the integrals in our study is set at 150 km, where the recombination still has an impact on the growth rate. To facilitate a comprehensive assessment of our equations across various experiments, we assume that recombination in the ionospheric $F$-region in the evening sector is negligible. This simplification allows us to maximize the observed growth rate and better identify the variations.

In our results, we have observed particularly rapid R-T growth rates occurring at altitudes ranging from 200 to 400 km in the post-sunset sector. These growth rates exhibit a strong dependence on both the PRE vertical drift and solar activity, which are in a good agreement with the simulations utilizing Equation 37 using the TIEGCM (Carter et al., 2014a, 2014b; Wu, 2015, 2017) and GAIA (Shinagawa et al., 2018) models. Several studies also suggest that the PRE provides a preferred condition for the development of the R-T instability (C. S. Huang & Hairston, 2015; Kil et al., 2009; Tsunoda et al., 2018). Concerning the R-T growth rates above 700 km at 284°E, which can be mapped to mid-latitude, we have discovered a contrasting feature of the solar activity effect compared to the growth rates below 400 km. Interestingly, Su et al. (2006) found that the irregularity occurrences in mid-latitude observed by ROCSAT-1 exhibit an inverse proportionality to solar activities within the range of 100–180 sfu. Several studies also suggested that the mid-latitude EPBs are associated with the Perkins instability (Perkins, 1973; Wang et al., 2019), not the R-T instability. Further investigation is required to explore the solar activity dependency of R-T growth rate when the flux-tubes pass through the mid-latitude ionosphere.

The seasonal and longitudinal distribution of R-T growth rate simulations using the coupled WAM-IPE successfully demonstrate a good agreement with previous satellite observations of EPBs and scintillations (e.g., Burke et al., 2004; Gentile et al., 2006; C. S. Huang et al., 2014; C. Y. Huang et al., 2022; Kil et al., 2009). However, there are small differences in certain seasons and at certain longitudes in the comparisons, largely associated with the *F* region zonal wind, as indicated in the simulations using TIEGCM (Wu, 2015). When compared with other simulation results, it is apparent that the simulation using the modified electrodynamics equations with WAM-IPE captures the morphological aspects of the R-T growth rate more reasonably and in correspondence with the EPBs climatology. Compared to results in Wu (2015) using the TIEGCM, the WAM-IPE results show variations of R-T growth rate within the longitudinal span of 0°–60°E around June solstice and strong day-to-day variations in all longitudes. The limitation in reproducing observed day-to-day variability of R-T growth rate in the TIEGCM can be attributed to the absence of day-to-day variation in perturbations from the low atmosphere, resulting in a less pronounced day-to-day ionospheric variation (Zhou et al., 2021). However, the growth rates calculated by WAM-IPE are fast between day 270–300 (October). The TIEGCM result around September equinox coincides more closely with the EPBs distribution observed by DMSP. This can be attributed to the strong PRE vertical drift observed in the WAM-IPE simulation during October (Figure 5b). When our results are compared with the R-T growth rate using GAIA (Shinagawa et al., 2018), the GAIA results show significant day-to-day variability; however, increased GAIA growth rate is not very clearly observed in the Atlantic region. This likely results from GAIA's utilization of a tilted dipole model, which significantly differs from the real magnetic field configuration in that specific region.

A term analysis is further carried out to investigate contributions of each component in Equation 36 to the R-T growth rate. The complete equations for the term analysis are denoted as $\Sigma^F_{x_0} E_{x_0} + K^{DF}_{x_0} - \Sigma^F_{c_0} E_{y_0}$, $\Sigma^F_{x_0} E_{x_0}$, $K^{DF}_{x}$, and $\Sigma^F_{c_0} E_{y_0}$ in Figures 6 and 7. Note that a negative value of $\Sigma^F_{c_0} E_{y_0}$ has a positive contribution to the R-T growth rate. The R-T growth rates at 284°E driven by various terms in Equation 36 are shown in Figures 6a–6d. The simulation conditions are the same as those in Figure 1. The negative values have been retained in the plots to demonstrate parameters that may suppress the generation of R-T growth rates. The results show that the $\Sigma^F_{x_0} E_{x_0}$ term controls the growth rate, whereas the contributions from the other two terms are minimal. This emphasizes significant differences between local and integrated theory of R-T instability. Kelley et al. (1979) compared the local theory of R-T growth rates of the gravitational and electric field-driven processes and found that for a 0.5 mV/m eastward electric field, the two sources of instability are equal at an altitude of 375 km. Below 375 km, the eastward electric field dominates, whereas above this altitude, the gravitational term dominates, exhibiting an exponential increase with altitude. Zargham and Seyler (1989) also suggested that when both gravity and electric field are included in the local theory of R-T instability, the growth rate in the collisional regime is determined by the electric field, while the growth rate in the inertial regime depends on the gravitational field. Defining the boundary between the collisional regime and inertial regime is approximately at around 500 km (Huba et al., 1985). Although, the $K^{DF}_{x}$ after 21 LT tends to increase with increasing altitude between 400 and 600 km, it does not dominate the growth rate in the nighttime as that based on the local theory. Haerendel (1973) and Sultan (1996) suggested that the altitude of the collisional/inertial regime boundary is increased for flux tube theory due to the limitation value of flux tube integrated collision frequency above a certain altitude. This indicates that in the equatorial region, the integrated theory of R-T instability is dominated by the electric field and does not transition to being controlled by gravity with increases in altitude.

Figures 7a–7d reveals the longitudinal variation of the maximum growth rate between apex altitudes of 200 and 400 km driven by various parameters in Equation 36 on the two equinoxes (20 March and 20 September) and the two solstices (20 June and 20 December) of 2013. It is obvious that the main contribution to the R-T growth rate comes from the $\Sigma^F_{x_0} E_{x_0}$ term at almost all longitudes throughout all these seasons, and the trends of the four quantities at the March and September equinoxes are quite similar. However, $K^{DF}_{x_0}$ predominates in the growth rate

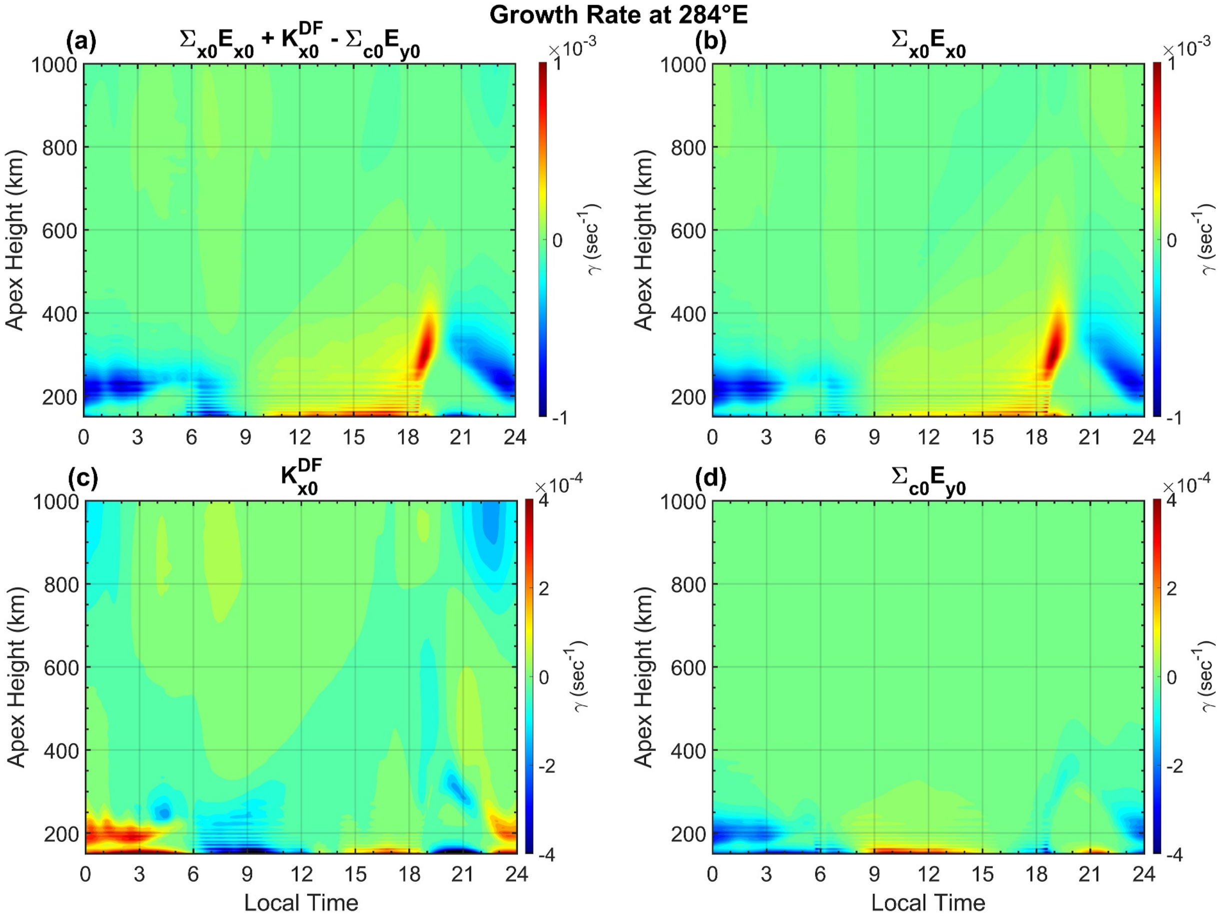

**Figure 6.** The Rayleigh-Taylor growth rate at 284°E driven by (a) $\Sigma_{x_0}^F E_{x_0} + K_{x_0}^{DF} - \Sigma_{c_0}^F E_{y_0}$, (b) $\Sigma_{x_0}^F E_{x_0}$, (c) $K_{x_0}^{DF}$, and (d) $\Sigma_{c_0}^F E_{y_0}$ in the parentheses of Equation 36 on 20 March. The $F_{10.7}$ and the $Kp$ retain the same values as those in Figure 1. Note that the top scales in (c) and (d) are different from that in (a) and (b).

within the longitude range of 75°E∼105°E (Figure 7b). This could be due to a strong downward drift in that region in the evening sector, leading to enhanced recombination and resulting in lower ion densities as well as lower conductivities (Kil et al., 2009; Kil & Oh, 2011; Wu, 2015). The effect of $\Sigma_{x_0}^F E_{x_0}$ at the June solstice is lowest compared to that in other seasons at most longitudes. Previous study has shown that the PRE signature and eastward zonal drift are considered to be weakest in the June solstice compared to that in other seasons at Jicamarca longitude (e.g., Fejer et al., 1999; Fesen et al., 2000; Scherliess & Fejer, 1999; Smith et al., 2016). However, the seasonal pattern of PRE is different at different longitudes (Abdu et al., 1981; Batista et al., 1986; Fejer et al., 2008), which can also be found in Figure 5b. Further examination is needed to explore the relationship among the $\Sigma_{x_0}^F E_{x_0}$ and the PRE at all longitudes. Interestingly, the growth rate driven by $K_{x_0}^{DF}$ appears to be greater at the June solstice than in other seasons. Since the lower boundary of the integrals is 150 km, the $\frac{\sigma_p d_1^2}{D} u_{e_2}$ term will be greater than the $\left(\sigma'_H - \frac{\sigma'_p \overrightarrow{\boldsymbol{d_1}} \cdot \overrightarrow{\boldsymbol{d_2}}}{D}\right) u_{e_1}$ term, which suggests that the meridional wind component might significantly impact the dynamo term. However, T. Maruyama (1988) suggests that the meridional wind enhances the field-line integrated Pedersen conductivity but reduces the growth rate of the generalized R-T instability. Zalesak and Huba (1991) also found that the instability can be completely stabilized for a sufficiently strong meridional wind. Conversely, Devasia et al. (2002) and Jyoti et al. (2004) found that under certain circumstances equatorward neutral winds appeared to be needed for ESF to develop. If the meridional wind dynamo becomes crucial during the solstice seasons, a similar phenomenon should be observed at the December solstice; however, this is not evident in our results. Further research is needed to investigate the relationship between the

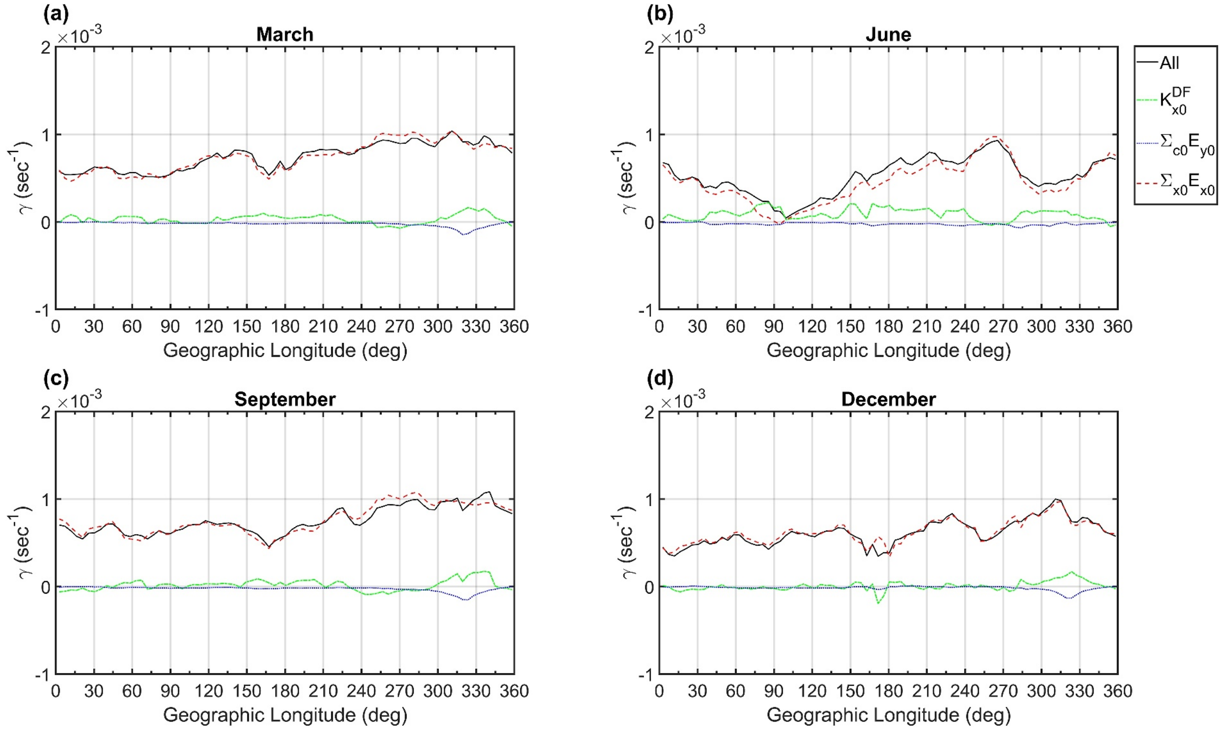

**Figure 7.** Maximum Rayleigh-Taylor (R-T) growth rate observed between 200 and 400 km at different longitude during the time span from 1800 local time (LT) to 2400 LT on (a) 20 March, (b) 20 June, (c) 20 September, and (d) 20 December. The black solid lines, red dashed lines, green dashed lines, and blue dotted lines represent the R-T growth rate driven by various parameters in Equation 36. The $F_{10.7}$ and the $Kp$ remain consistent with those in Figure 1.

thermospheric wind and R-T instability. In term of the contribution of $\Sigma_{c_0}^{F} E_{y_0}$, it exhibits a minor impact on the growth rate, most notably around 330°E at the two equinoxes and the December solstice, as well as within the longitude region between 150°E~330°E at the June solstice.

## 6. Conclusion and Future Work

We propose a new expression for calculating the linear R-T instability based on the flux-tube integrated theory, and subsequently validate this expression using the coupled WAM-IPE model. Compared to the expression proposed by Sultan (1996), the expression in this study incorporates the modified equations of electrodynamics due to the distortions of geomagnetic field. Through the mapping of the field-line-integrated calculations onto the Modified Magnetic Apex coordinate system, the electrodynamic equations can be expressed in two dimensions in magnetic latitude and longitude, and have been easily integrated into WAM-IPE for the convenient estimation of the R-T growth rate.

In this study, some assumptions were made to simplify the calculations. First, the loss term is neglected because the integration boundary starts at 150 km. Although in the lower $F$ region, the loss process does have some influence on the recombination rate and the growth rate, eliminating this term facilitates our observation of the similarities between the variations of R-T instability growth rate and the vertical drift. The second assumption is that electric field perturbations are confined to the zonal direction, so that ion density perturbations are produced only by meridional $\vec{E} \times \vec{B}$ drifts. This allows us to calculate growth rates independently at each apex altitude, which corresponds to the treatments of many earlier studies (e.g., Kelley, 2009; Ossakow, 1981; Sultan, 1996; Zalesak & Ossakow, 1982). The third assumption is that effects of Hall conductance can be neglected. If night-time $E$ region ion densities are large enough, the effects of Hall conductance on the perturbation electric field could be significant, but inclusion of Hall conductivity would greatly complicate the theoretical analysis. It should be considered in future studies. The fourth assumption confines the scope of our study to the perturbations in the $F$ region. Ion velocities in the $E$ region do not follow the $\frac{\vec{E}\times\vec{B_0}}{B_0^2}$ velocity, and so Equations 12, 14, and 17 are not applicable there. Our assumption is valid if the $E$ region contributions to perturbations of field-line-integrated conductivities are negligible. The analysis is therefore valid only if perturbation of the nighttime $E$ region Pedersen and Hall conductivities are sufficiently small, which allows us to simplify Equation 29. The last significant assumption is that the electron density changes by the same fraction at all points along a field line above 150 km. This allows the approximation of the fractional perturbations of dynamo current and Pedersen conductance to be similar to that of field-line integrated ion content since the Pedersen conductivity is proportional to the electron density in the $F$ region. Consequently, the perturbations of the dynamo current and the Pedersen conductance can be simplified.

Investigations of diurnal variations, dependencies on PRE vertical drift, and responses to solar activity are carried out. The seasonal and longitudinal variation during 2013 of R-T growth rate have been investigated. While the distributions and variations differ slightly from other simulation, the morphology of growth rate in this study aligns more closely with the in-situ measurement of EPBs and with scintillations observed by satellites during similar solar activity periods. In addition, we also compared the contributions of various parameters in the expression to the growth rate, which shows that the $\Sigma_{x_0}^{F} E_{x_0}$ term always dominates the growth rate. These results agree well with previous studies, which suggests our expression for calculating R-T instability growth rates using the coupled WAM-IPE model is valid and appropriate.

Additionally, our results show that the simulation varies with the day-to-day variation of ionospheric structure. This suggests that using our expression in conjunction with WAM-IPE is suitable for studying the day-to-day variability of the R-T growth rate. The free run WAM-IPE cannot perfectly reproduce the real ionosphere structure; thus, it may not accurately capture the condition leading to R-T instability and the EPB occurrence. However, we will aim to incorporate this expression into the operational WAM-IPE, which will enable the exploration of the connection between R-T instability growth rate and the EPB occurrence/scintillations. The ability of operational WAM-IPE to forecast ionospheric and thermospheric conditions 2 days in advance even offers great potential for establishing alerts and warnings for the formation of EPBs in the future.

## Appendix A: Investigation of Assumption

According to Equation 29, the main causal mechanism of R-T instability is the perturbation electric field in $x$ direction, which causes the $F$ region ions and electrons in a flux tube all to move with respect to apex height ($h_A$). Therefore, the changes of the ion density ($n$) due to the electric field perturbation are associated with the movements, so that,

$$n' = \left(\frac{dn}{dh_A}\right) h'_A \tag{A1}$$

In the $F$ region, where the ion-neutral collision frequency $\nu_i$ is small in comparison with the ion gyrofrequency $\omega_i$, the Pedersen conductance above 150 km can be written as,

$$\Sigma_x = \int_{S(150)}^{N(150)} \sigma_p \frac{{d_1}^2}{D} ds \cong \int_{S(150)}^{N(150)} n \frac{e}{B} \frac{\nu_i}{\omega_i} \frac{{d_1}^2}{D} ds \tag{A2}$$

where $e$ is ion charge, $\nu_i$ is ion collision frequency, and $\omega_i$ is ion gyrofrequency. The perturbation in $\Sigma_x$ then can be described as follows,

$$\Sigma'_x = \int_{S(150)}^{N(150)} \frac{dn}{dh_A} \frac{e}{B} \frac{\nu_i}{\omega_i} \frac{{d_1}^2}{D} h'_A ds \tag{A3}$$

Similarly, the perturbations of the field-line-integrated ion content $\eta$ and dynamo current density $K_x^D$ can be expressed as follows,

$$\eta' = \int_{S(150)}^{N(150)} \frac{dn}{dh_A} \frac{1}{B} h'_A ds \tag{A4}$$

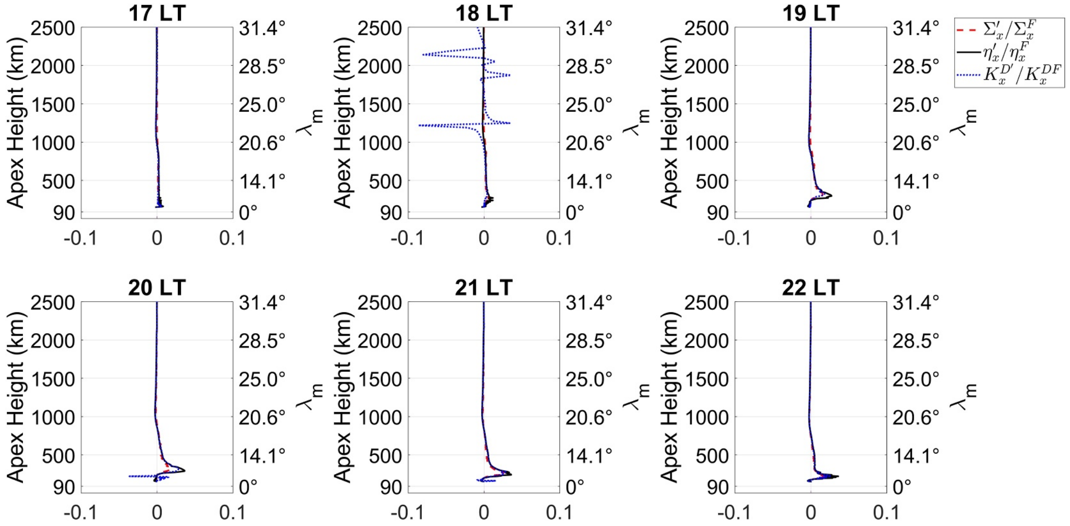

**Figure A1.** The fractional perturbations of $\Sigma_x$ (red dashed line), $\eta$ (black line), and $K_x^D$ (blue dotted line) as a function of apex height at 284°E from 17 local time (LT) to 22 LT, respectively. The simulation is driven by $F_{10.7}$ of 120 sfu and $Kp$ of 1.

$$K_x^{D'} = B_{e_3} \cos \lambda_m \int_{S(150)}^{N(150)} \left[ \frac{dn}{dh_A} \frac{e}{B} \frac{\nu_i}{\omega_i} \frac{d_1^2}{D} {h'}_A u_{e_2} + \left( \sigma_H - \frac{dn}{dh_A} \frac{e}{B} \frac{\nu_i}{\omega_i} \frac{\overrightarrow{\boldsymbol{d_1}} \cdot \overrightarrow{\boldsymbol{d_2}}}{D} h'_A \right) u_{e_1} + \frac{dn}{dh_A} \frac{m_i \overrightarrow{\boldsymbol{e_2}} \cdot \overrightarrow{\boldsymbol{g}}}{B_{e_3} B} h'_A \right] ds \quad \text{(A5)}$$

The Expressions A3–A5 are similar to the expressions for unprimed $\Sigma_x$, $\eta$, and $K_x^D$, respectively, except that Equations A3–A5 have replaced $n$ in the integrals by $\left(\frac{dn}{dh_A}\right) h'_A$, where $h'_A$ is a constant along the field line. If $\frac{dn}{dh_A}$ varies along the field line in a similar manner as $n$, then the fractional perturbations in Equation 33 will all be similar. To test whether they are similar, the altitude change between apex points was used to calculate the fractional perturbations show in Figure A1.

## Data Availability Statement

The WAM-IPE simulation results evaluated in this study are available at C. Y. Huang et al. (2024).

**Acknowledgments**
The authors sincerely appreciate Dr. Qian Wu for the HAO internal review and the helpful detailed comments from the reviewers. Chun-Yen Huang and Timothy J. Fuller-Rowell were supported by NSF Space Weather with Quantification of Uncertainties program under Grant AGS 2028032. Arthur D. Richmond's contributions were funded in part by NASA Award No. 80NSSC17K0719. Jann-Yenq Liu was granted supported from the National Science and Technology Council (NSTC) Grant NSTC 112-2123-M-008-003. This material is based upon work supported by the NSF National Center for Atmospheric Research, which is a major facility sponsored by the U.S. National Science Foundation under Cooperative Agreement No. 1852977. High-performance computing support from Cheyenne was provided by NCAR's Computational and Information Systems Laboratory. The source code for WAM-IPE can be downloaded at the following GitHub repository (https://github.com/CU-SWQU/GSMWAM-IPE).

## References

Abdu, M. A., Bittencourt, J. A., & Batista, I. S. (1981). Magnetic declination control of the equatorial F region dynamo electric field development and spread F. *Journal of Geophysical Research*, *86*(A13), 11443–11446. https://doi.org/10.1029/ja086ia13p11443

Akmaev, R. A., Fuller-Rowell, T. J., Wu, F., Forbes, J. M., Zhang, X., Anghel, A. F., et al. (2008). Tidal variability in the lower thermosphere: Comparison of Whole AtmosphereModel (WAM) simulations with observations from TIMED. *Geophysical Research Letters*, *35*(3), L03810. https://doi.org/10.1029/2007GL032584

Basu, S., Kudeki, E., Basu, S., Valladares, C. E., Weber, E. J., Zengingonul, H. P., et al. (1996). Scintillations, plasma drifts, and neutral winds in the equatorial ionosphere after sunset. *Journal of Geophysical Research*, *101*(A12), 26795–26809. https://doi.org/10.1029/96JA00760

Batista, I., Abdu, M., & Bittencourt, J. (1986). Equatorial F region vertical plasma drifts: Seasonal and longitudinal asymmetries in the American sector. *Journal of Geophysical Research*, *91*(A11), 12055–12064. https://doi.org/10.1029/JA091iA11p12055

Bittencourt, J. A., & Abdu, M. A. (1981). Theoretical comparison between apparent and real vertical ionization drift velocities in the equatorial F-region. *Journal of Geophysical Research*, *86*(A4), 2451–2455. https://doi.org/10.1029/JA086iA04p02451

Booker, H. G., & Wells, H. G. (1938). Scattering of radio waves by the F-region of the ionosphere. *Terrestrial Magnetism and Atmospheric Electricity*, *43*(3), 249–256. https://doi.org/10.1029/TE043i003p00249

Burke, W. J., Gentile, L. C., Huang, C. Y., Valladares, C. E., & Su, S. Y. (2004). Longitudinal variability of equatorial plasma bubbles observed by DMSP and ROCSAT-1. *Journal of Geophysical Research*, *109*(A12), A12301. https://doi.org/10.1029/2004JA010583

Carter, B. A., Retterer, J. M., Yizengaw, E., Groves, K., Caton, R., McNamara, L., et al. (2014a). Geomagnetic control of equatorial plasma bubble activity modeled by the TIEGCM with Kp. *Geophysical Research Letters*, *41*(15), 5331–5339. https://doi.org/10.1002/2014GL060953

Carter, B. A., Yizengaw, E., Retterer, J. M., Francis, M., Terkildsen, M., Marshall, R., et al. (2014b). An analysis of the quiet time day-to-day variability in the formation of postsunset equatorial plasma bubbles in the Southeast Asian region. *Journal of Geophysical Research: Space Physics*, *119*(4), 3206–3223. https://doi.org/10.1002/2013JA019570

Devasia, C. V., Jyoti, N., Viswanathan, K. S., Tiwari, D., & Sridharan, R. (2002). On the plausible leakage of thermospheric meridional winds with equatorial spread F. *Journal of Atmospheric and Solar-Terrestrial Physics*, *64*(1), 1–12. https://doi.org/10.1016/S1364-6826(01)00089-X

Dungey, J. W. (1956). Convective diffusion in the equatorial F-region. *Journal of Atmospheric and Terrestrial Physics*, *9*(5–6), 304–310. https://doi.org/10.1016/0021-9169(56)90148-9

Fang, T.-W., Akmaev, R., Fuller-Rowell, T., Wu, F., Maruyama, N., & Millward, G. (2013). Longitudinal and day-to-day variability in the ionosphere from lower atmosphere tidal forcing. *Geophysical Research Letters*, *40*(11), 2523–2528. https://doi.org/10.1002/grl.50550

Fang, T.-W., Kubaryk, A., Goldstein, D., Li, Z., Fuller-Rowell, T., Millward, G., et al. (2022). Space weather environment during the SpaceX Starlink satellite loss in February 2022. *Space Weather*, *20*(11), e2022SW003193. https://doi.org/10.1029/2022SW003193

Farley, D. T., Balsey, B. B., Woodman, R. F., & McClure, J. P. (1970). Equatorial spread F: Implications of VHF radar observations. *Journal of Geophysical Research*, *75*(34), 7199–7216. https://doi.org/10.1029/JA075i034p07199

Farley, D. T., Bonelli, E., Fejer, B. G., & Larsen, M. F. (1986). The prereversal enhancement of the zonal electric field in the equatorial ionosphere. *Journal of Geophysical Research*, *91*(A12), 13723–13728. https://doi.org/10.1029/ja091ia12p13723

Fejer, B. G., Jensen, J., & Su, S.-Y. (2008). Quiet time equatorial F region vertical plasma drift model derived from ROCSAT-1 observations. *Journal of Geophysical Research*, *113*(A5), A05304. https://doi.org/10.1029/2007JA012801

Fejer, B. G., Scherliess, L., & de Paula, E. R. (1999). Effects of the vertical plasma drift velocity on the generation and evolution of equatorial spread F. *Journal of Geophysical Research*, *104*(A9), 19859–19869. https://doi.org/10.1029/1999JA900271

Fesen, C. G., Crowley, G., Roble, R. G., Richmond, A. D., & Fejer, B. G. (2000). Simulation of the pre-reversal enhancement in the low latitude vertical ion drifts. *Geophysical Research Letters*, *27*(13), 1851–1854. https://doi.org/10.1029/2000gl000061

Fukao, S., Kelley, M. C., Shirakawa, T., Takami, T., Yamameto, M., Tsuda, T., & Kato, S. (1991). Turbulent upwelling of the midlatitude ionosphere: 1. Observational results by the MU radar. *Journal of Geophysical Research*, *96*(A3), 3725–3746. https://doi.org/10.1029/90ja02253

Fuller-Rowell, T. J., Wu, F., Akmaev, R., Fang, T.-W., & Araujo-Pradere, E. (2010). A whole atmosphere model simulation of the impact of a sudden stratospheric warming on thermosphere dynamics and electrodynamics. *Journal of Geophysical Research*, *115*(A10), A00G08. https://doi.org/10.1029/2010JA015524

Fuller-Rowell, T. J., Akmaev, R. A., Wu, F., Anghel, A., Maruyama, N., Anderson, D. N., et al. (2008). Impact of terrestrial weather on the upper atmosphere. *Geophysical Research Letters*, *35*(9), L09808. https://doi.org/10.1029/2007GL032911

Gauss, C. F. (1838). Allgemeine Theorie des Erdmagnetismus. In C. F. Gauss & W. Weber (Eds.), *Resultate aus den Beobachtungen des magnetischen Vereins im Jahre* (pp. 1–57). Weidmannsche Buchhandlung.

Gentile, L. C., Burke, W. J., & Rich, F. J. (2006). A global climatology for equatorial plasma bubbles in the topside ionosphere. *Annales Geophysicae*, *24*(1), 163–172. https://doi.org/10.5194/angeo-24-163-2006

Glassmeier, K. H., & Tsurutani, B. T. (2014). Carl Friedrich Gauss-general theory of terrestrial magnetism - A revised translation of the German text. *History of Geo- and Space Sciences*, *5*(1), 11–62. https://doi.org/10.5194/hgss-5-11-2014

Haerendel, G. (1973). *Theory of equatorial spread-F*. Max Planck Institute for Extraterrestrial Physics.

Haerendel, G., Eccles, J. V., & Cakir, S. (1992). Theory for modeling the equatorial evening ionosphere and the origin of the shear in the horizontal plasma flow. *Journal of Geophysical Research*, *97*(A2), 1209–1223. https://doi.org/10.1029/91ja02226

Hanson, W. B., Cragin, B. L., & Dennis, A. (1986). The effect of vertical drift on the equatorial F-region stability. *Journal of Atmospheric and Terrestrial Physics*, *48*(3), 205–212. https://doi.org/10.1016/0021-9169(86)90095-4

Hedin, A. E. (1991). Extension of the MSIS thermospheric model into the middle and lower atmosphere. *Journal of Geophysical Research*, *96*(A2), 1159–1172. https://doi.org/10.1029/90ja02125

Hu, S., & Bhattacharjee, A. (1999). Gradient drift instabilities and turbulence in the nighttime equatorial electrojet. *Journal of Geophysical Research*, *104*(A12), 28123–28132. https://doi.org/10.1029/1999ja900399

Huang, C. S., de La Beaujardiere, O., Roddy, P. A., Hunton, D. E., Liu, J. Y., & Chen, S. P. (2014). Occurrence probability and amplitude of equatorial ionospheric irregularities associated with plasma bubbles during low and moderate solar activities (2008–2012). *Journal of Geophysical Research: Space Physics*, *119*(2), 1186–1199. https://doi.org/10.1002/2013JA019212

Huang, C. S., & Hairston, M. R. (2015). The postsunset vertical plasma drift and its effects on the generation of equatorial plasma bubbles observed by the C/NOFS satellite. *Journal of Geophysical Research: Space Physics*, *120*(3), 2263–2275. https://doi.org/10.1002/2014JA020735

Huang, C. Y., Fang, T. W., Richmond, A., Fuller-Rowell, T., & Liu, J. Y. (2024). New expression of the field-line integrated Rayleigh-Taylor instability growth rate [Dataset]. *Zenodo*. https://doi.org/10.5281/zenodo.10946780

Huang, C. Y., Liu, J. Y., Chang, F. Y., Lin, C. Y., Chao, C. K., Chang, L. C., & Lin, C. Y. (2022). Instantaneous amplitude of low-latitude ionospheric irregularities probed by ROCSAT-1, DEMETER, and FORMOSAT-7/COSMIC-2. *Advances in Space Research*, *70*(3), 723–732. https://doi.org/10.1016/j.asr.2022.05.024

Huba, J. D. (2022). Generalized Rayleigh-Taylor instability: Ion inertia, acceleration forces, and E region drivers. *Journal of Geophysical Research: Space Physics*, *127*(6), e2022JA030474. https://doi.org/10.1029/2022JA030474

Huba, J. D., Hassam, A. B., Schwartz, I. B., & Keskinen, M. J. (1985). Ionospheric turbulence: Interchange instability and chaotic fluid behavior. *Geophysical Research Letters*, *12*(1), 65–68. https://doi.org/10.1029/gl012i001p00065

Hysell, D. L. (2000). An overview and synthesis of plasma irregularities in equatorial spread F. *Journal of Atmospheric and Solar-Terrestrial Physics*, *62*(12), 1037–1056. https://doi.org/10.1016/s1364-6826(00)00095-x

Hysell, D. L., & Chau, J. L. (2023). Aperture synthesis imaging of ionospheric irregularities using time diversity MIMO radar. *Radio Science*, *58*(9), e2023RS007765. https://doi.org/10.1029/2023RS007765

Hysell, D. L., & Kudeki, E. (2004). Collisional shear instability in the equatorial F region ionosphere. *Journal of Geophysical Research*, *109*(A11), A11301. https://doi.org/10.1029/2004JA010636

Hysell, D. L., Larsen, M. F., Swenson, C. M., & Wheeler, T. F. (2006). Shear flow effects at the onset of equatorial spread F. *Journal of Geophysical Research*, *111*(A11), A11317. https://doi.org/10.1029/2006JA011963

Jayachandran, B., Balan, N., Rao, P. B., Sastri, J. H., & Bailey, G. J. (1993). HF Doppler and ionosonde observations on the onset conditions of equatorial spread F. *Journal of Geophysical Research*, *98*(A8), 13741–13750. https://doi.org/10.1029/93ja00302

Jyoti, N., Devasia, C. V., Sridharan, R., & Tiwari, D. (2004). Threshold height (h'F)c for the meridional wind to play a deterministic role in the bottom side equatorial spread F and its dependence on solar activity. *Geophysical Research Letters*, *31*(12), L12809. https://doi.org/10.1029/2004GL019455

Kelley, M. C. (2009). *The Earth's ionosphere: Electrodynamics and plasma physics* (2nd ed.). Elsevier.

Kelley, M. C., Baker, K. D., & Ulwick, J. C. (1979). Late time barium cloud striations and their possible relationship to equatorial spread F. *Journal of Geophysical Research*, *84*(A5), 1898–1904. https://doi.org/10.1029/ja084ia05p01898

Kelley, M. C., & Fukao, S. (1991). Turbulent upwelling of the midlatitude ionosphere: 2. Theoretical framework. *Journal of Geophysical Research*, *96*(A3), 3747–3753. https://doi.org/10.1029/90ja02252

Kelley, M. C., Larsen, M. F., LaHoz, C., & McClure, J. P. (1981). Gravity wave initiation of equatorial spread F: A case study. *Journal of Geophysical Research*, *86*(A11), 9087–9100. https://doi.org/10.1029/ja086ia11p09087

Keskinen, M. J., Mitchell, H. G., Fedder, J. A., Satyanarayana, P., Zalesak, S. T., & Huba, J. D. (1988). Nonlinear evolution of the Kelvin-Helmholtz instability in the high-latitude ionosphere. *Journal of Geophysical Research*, *93*(A1), 137–152. https://doi.org/10.1029/ja093ia01p00137

Keskinen, M. J., & Ossakow, S. L. (1983). Theories of high-latitude ionospheric irregularities: A review. *Radio Science*, *18*(6), 1077–1091. https://doi.org/10.1029/RS018i006p01077

Kil, H., & Oh, S.-J. (2011). Dependence of the evening prereversal enhancement of the vertical plasma drift on geophysical parameters. *Journal of Geophysical Research*, *116*(A5), A05311. https://doi.org/10.1029/2010JA016352

Kil, H., Paxton, L. J., & Oh, S. J. (2009). Global bubble distribution seen from ROCSAT-1 and its association with the evening prereversal enhancement. *Journal of Geophysical Research*, *114*(A6), A06307. https://doi.org/10.1029/2008JA013672

Klevans, E. H., & Imel, G. (1978). E-region coupling effects on the Perkins spread F instability. *Journal of Geophysical Research*, *83*(A1), 199–202. https://doi.org/10.1029/ja083ia01p00199

Lee, C. C. (2006). Examine the local linear growth rate of collisional Rayleigh-Taylor instability during solar maximum. *Journal of Geophysical Research*, *111*(A11), A11313. https://doi.org/10.1029/2006JA011925

Linson, L. M., & Workman, J. B. (1970). Formation of striations in ionospheric plasma clouds. *Journal of Geophysical Research*, *75*(16), 3211–3219. https://doi.org/10.1029/JA075i016p03211

Maruyama, N., Sun, Y.-Y., Richards, P. G., Middlecoff, J., Fang, T.-W., Fuller-Rowell, T. J., et al. (2016). A new source of the midlatitude ionospheric peak density structure revealed by a new Ionosphere-Plasmasphere model. *Geophysical Research Letters*, *43*(6), 2429–2435. https://doi.org/10.1002/2015GL067312

Maruyama, T. (1988). A diagnostic model for equatorial spread F, 1, Model description and application to electric field and neutral wind effects. *Journal of Geophysical Research*, *93*(14), 14611–14622. https://doi.org/10.1029/ja093ia12p14611

McIlwain, C. E. (1961). Coordinates for mapping the distribution of magnetically trapped particles. *Journal of Geophysical Research*, *66*(11), 3681–3691. https://doi.org/10.1029/jz066i011p03681

Mendillo, M., Baumgardner, J., Pi, X., Sultan, P. J., & Tsunoda, R. (1992). Onset conditions for equatorial spread F. *Journal of Geophysical Research*, *97*(A9), 13865–13876. https://doi.org/10.1029/92JA00647

Obana, Y., Maruyama, N., Shinbori, A., Hashimoto, K. K., Fedrizzi, M., Nosé, M., et al. (2019). Response of the ionosphere-plasmasphere coupling to the September 2017 storm: What erodes the plasmasphere so severely? *Space Weather*, *17*(6), 861–876. https://doi.org/10.1029/2019SW002168

Ossakow, S. L. (1979). Ionospheric irregularities. https://doi.org/10.1029/RG017i004p00521

Ossakow, S. L. (1981). Spread F theories—A review. *Journal of Atmospheric and Terrestrial Physics*, *43*(5–6), 437–452. https://doi.org/10.1016/0021-9169(81)90107-0

Ossakow, S. L., Zalesak, S. T., McDonald, B. E., & Chaturvedi, P. K. (1979). Nonlinear equatorial spread F: Dependence on altitude of the F peak and bottomside background electron density gradient scale length. *Journal of Geophysical Research*, *84*(A1), 17–29. https://doi.org/10.1029/JA084iA01p00017

Otsuka, Y., Onoma, F., Shiokawa, K., Ogawa, T., Yamamoto, M., & Fukao, S. (2007). Simultaneous observations of nighttime medium-scale traveling ionospheric disturbances and *E*-region field-aligned irregularities at mid-latitude. *Journal of Geophysical Research*, *112*(A6), A06317. https://doi.org/10.1029/2005JA011548

Pedatella, N. M., Fang, T.-W., Jin, H., Sassi, F., Schmidt, H., Chau, J. L., et al. (2016). Multimodel comparison of the ionosphere variability during the 2009 sudden stratosphere warming. *Journal of Geophysical Research: Space Physics*, *121*(7), 7204–7225. https://doi.org/10.1002/2016JA022859

Perkins, F. (1973). Spread F and ionospheric currents. *Journal of Geophysical Research*, *78*(1), 218–226. https://doi.org/10.1029/ja078i001p00218

Qian, L., Burns, A., Emery, B. A., Foster, B. T., Lu, G., Maute, A., et al. (2014). The NCAR TIE-GCM: A community model of the coupled thermosphere/ionosphere system. In J. Huba, R. Schunk, & G. Khazanov (Eds.), *Modeling the ionosphere-thermosphere system* (pp. 73–84). John Wiley & Sons. https://doi.org/10.1002/9781118704417.ch7

Rathod, C., Srinivasan, B., Scales, W., & Kunduri, B. (2021). Investigation of the gradient drift instability as a cause of density irregularities in subauroral polarization streams. *Journal of Geophysical Research: Space Physics*, *126*(5), e2020JA029027. https://doi.org/10.1029/2020JA029027

Richards, P. G., Bilitza, D., & Voglozin, D. (2010). Ion density calculator (IDC): A new efficient model of ionospheric ion densities. *Radio Science*, *45*(5), RS5007. https://doi.org/10.1029/2009RS004332

Richards, P. G., Fennelly, J. A., & Torr, D. G. (1994). EUVAC: A solar EUV flux model for aeronomic calculations. *Journal of Geophysical Research*, *99*(A5), 8981–8992. https://doi.org/10.1029/94JA00518

Richards, P. G., & Torr, D. G. (1996). The field line interhemispheric plasma model. In R. W. Schunk (Ed.), *STEP: Handbook of ionospheric models* (pp. 207–216). Utah State Univ.

Richmond, A. D. (1995). Ionospheric electrodynamics using magnetic apex coordinates. *Journal of Geomagnetism and Geoelectricity*, *47*(2), 191–212. https://doi.org/10.5636/jgg.47.191

Richmond, A. D., & Fang, T. W. (2015). Electrodynamics of the equatorial evening ionosphere: 2. Conductivity influences on convection, current, and electrodynamic energy flow. *Journal of Geophysical Research: Space Physics*, *120*(3), 2133–2147. https://doi.org/10.1002/2014JA020935

Richmond, A. D., Fang, T. W., & Maute, A. (2015). Electrodynamics of the equatorial evening ionosphere: 1. Importance of winds in different regions. *Journal of Geophysical Research: Space Physics*, *120*(3), 2118–2132. https://doi.org/10.1002/2014JA020934

Richmond, A. D., & Maute, A. (2013). Ionospheric electrodynamics modeling. In J. Huba, R. Schunk, & G. Khazanov (Eds.), *Modeling the ionosphere-thermosphere system*, *Geophys. Monogr. 201* (pp. 57–71). AGU. https://doi.org/10.1029/2012GM001331

Richmond, A. D., Ridley, E. C., & Roble, R. G. (1992). A thermosphere/ionosphere general circulation model with coupled electrodynamics. *Geophysical Research Letters*, *19*(6), 601–604. https://doi.org/10.1029/92GL00401

Rottger, J. (1973). Wavelike structures of large scale equatorial spread F irregularities. *Journal of Atmospheric and Terrestrial Physics*, *35*(6), 1195–1206. https://doi.org/10.1016/0021-9169(73)90016-0

Scherliess, L., & Fejer, B. G. (1999). Radar and satellite global equatorial F region vertical drift model. *Journal of Geophysical Research*, *104*(A4), 6829–6842. https://doi.org/10.1029/1999JA900025

Shinagawa, H., Jin, H., Miyoshi, Y., Fujiwara, H., Yokoyama, T., & Otsuka, Y. (2018). Daily and seasonal variations in the linear growth rate of the Rayleigh-Taylor instability in the ionosphere obtained with GAIA. *Progress in Earth and Planetary Science*, *5*(1), 16. https://doi.org/10.1186/s40645-018-0175-8

Smith, J. M., Rodrigues, F. S., Fejer, B. G., & Milla, M. A. (2016). Coherent and incoherent scatter radar study of the climatology and day-to-day variability of mean F region vertical drifts and equatorial spread F. *Journal of Geophysical Research: Space Physics*, *121*(2), 1466–1482. https://doi.org/10.1002/2015JA021934

Su, S. Y., Liu, C. H., Ho, H. H., & Chao, C. K. (2006). Distribution characteristics of topside ionospheric density irregularities: Equatorial versus midlatitude regions. *Journal of Geophysical Research*, *111*(A6), A06305. https://doi.org/10.1029/2005JA011330

Sultan, P. J. (1996). Linear theory and modeling of the Rayleigh-Taylor instability leading to the occurrence of equatorial spread F. *Journal of Geophysical Research*, *101*(A12), 26875–26891. https://doi.org/10.1029/96ja00682

Sun, Y.-Y., Matsuo, T., Maruyama, N., & Liu, J.-Y. (2015). Field-aligned neutral wind bias correction scheme for global ionospheric modeling at midlatitudes by assimilating FORMOSAT-3/COSMIC hmF2 data under geomagnetically quiet conditions. *Journal of Geophysical Research: Space Physics*, *120*(4), 3130–3149. https://doi.org/10.1002/2014JA020768

Tsunoda, R. T. (1981). Time evolution and dynamics of equatorial backscatter plumes, 1, Growth phase. *Journal of Geophysical Research*, *86*(A1), 139–149. https://doi.org/10.1029/ja086ia01p00139

Tsunoda, R. T. (1985). Control of the seasonal and longitudinal occurrence of equatorial. scintillations by the longitudinal gradient in integrated E region Pedersen conductivity. *Journal of Geophysical Research*, *90*(A1), 447–456. https://doi.org/10.1029/JA090iA01p00447

Tsunoda, R. T., Saito, S., & Nguyen, T. T. (2018). Post-sunset rise of equatorial F layer—Or upwelling growth. *Progress in Earth and Planetary Science*, *22*(1), 5. https://doi.org/10.1186/s40645-018-0179-4

Wang, N., Guo, L., Ding, Z., Zhao, Z., Xu, Z., Xu, T., & Hu, Y. (2019). Longitudinal differences in the statistical characteristics of ionospheric spread-F occurrences at midlatitude in Eastern Asia. *Earth Planets and Space*, *71*(1), 47. https://doi.org/10.1186/s40623-019-1026-6

Weimer, D. R. (2005). Improved ionospheric electrodynamic models and application to calculating Joule heating rates. *Journal of Geophysical Research*, *110*(A5), A05306. https://doi.org/10.1029/2004JA010884

Wu, Q. (2015). Longitudinal and seasonal variation of the equatorial flux tube integrated Rayleigh-Taylor instability growth rate. *Journal of Geophysical Research: Space Physics*, *120*(9), 7952–7957. https://doi.org/10.1002/2015JA021553

Wu, Q. (2017). Solar effect on the Rayleigh-Taylor instability growth rate as simulated by the NCAR TIEGCM. *Journal of Atmospheric and Solar-Terrestrial Physics*, *156*, 97–102. https://doi.org/10.1016/j.jastp.2017.03.007

Zalesak, S. T., & Huba, J. D. (1991). Effect of meridional winds on the development of equatorial spread F. *Eos, Transactions American Geophysical Union*, *72*, 211.

Zalesak, S. T., & Ossakow, S. L. (1982). *On the prospect for artificially inducing equatorial spread F*. Memo. Rep. 4899. Nav. Res. Lab.

Zargham, S., & Seyler, C. E. (1989). Collisional and inertial dynamics of the ionospheric interchange instability. *Journal of Geophysical Research*, *94*(A7), 9009–9027. https://doi.org/10.1029/ja094ia07p09009

Zhou, X., Yue, X., Liu, H.-L., Lu, X., Wu, H., Zhao, X., & He, J. (2021). A comparative study of ionospheric day-to-day variability over Wuhan based on ionosonde measurements and model simulations. *Journal of Geophysical Research: Space Physics*, *126*(3), e2020JA028589. https://doi.org/10.1029/2020JA0285895